

---

This is an electronic reprint of the original article.  
This reprint may differ from the original in pagination and typographic detail.

Warnecke, J.; Korpi-Lagg, M. J.; Rheinhardt, M.; Viviani, M.; Prabhu, A.

**Small-scale and large-scale dynamos in global convection simulations of solar-like stars**

*Published in:*  
Astronomy and Astrophysics

*DOI:*  
[10.1051/0004-6361/202451085](https://doi.org/10.1051/0004-6361/202451085)

Published: 01/04/2025

*Document Version*  
Publisher's PDF, also known as Version of record

*Published under the following license:*  
CC BY

*Please cite the original version:*  
Warnecke, J., Korpi-Lagg, M. J., Rheinhardt, M., Viviani, M., & Prabhu, A. (2025). Small-scale and large-scale dynamos in global convection simulations of solar-like stars. *Astronomy and Astrophysics*, 696, 1-20. Article A93. <https://doi.org/10.1051/0004-6361/202451085>

# Small-scale and large-scale dynamos in global convection simulations of solar-like stars

J. Warnecke<sup>1,2,\*</sup>, M. J. Korpi-Lagg<sup>1,2,3</sup>, M. Rheinhardt<sup>1</sup>, M. Viviani<sup>2,4</sup>, and A. Prabhu<sup>2,5</sup>

<sup>1</sup> Department of Computer Science, Aalto University, PO Box 15400, FI-00 076 Espoo, Finland

<sup>2</sup> Max-Planck-Institut für Sonnensystemforschung, Justus-von-Liebig-Weg 3, D-37077 Göttingen, Germany

<sup>3</sup> Nordita, KTH Royal Institute of Technology & Stockholm University, Hannes Alfvéns väg 12, SE-11419 Stockholm, Sweden

<sup>4</sup> Wish s.r.l., Via Venezia 24, 87036 Rende, (CS), Italy

<sup>5</sup> Sensirion Connected Solutions, Laubisrütistrasse 50, 8712 Stäfa, Switzerland

Received 12 June 2024 / Accepted 14 December 2024

## ABSTRACT

**Context.** It has recently been shown numerically that a small-scale dynamo (SSD) instability might be possible in solar-like low magnetic Prandtl number plasmas. It was proposed that the presence of SSD might have a significant effect on the dynamics of the large-scale dynamo (LSD) in stellar convection zones. The simultaneous study of these two dynamos, SSD and LSD, in a global magnetohydrodynamic model requires high-resolution simulations and large amounts of computational resources.

**Aims.** Starting from a well-studied global convective dynamo model that produces cyclic magnetic fields, we systematically increased the resolution and lowered the diffusivities to enter the regime of Reynolds numbers that enable the excitation of SSD in addition to the LSD. We studied the change in the properties of convection, generated differential rotation profiles, and LSD solutions due to the presence of SSD.

**Methods.** We performed semiglobal convective dynamo simulations in a spherical wedge with the Pencil Code. The resolutions of the models were increased in four steps by a total factor of 16 to achieve maximum fluid and magnetic Reynolds numbers of above 500.

**Results.** We found that differential rotation is strongly quenched by the presence of the LSD and SSD. Even though the small-scale magnetic field only mildly decreases with increasing Reynolds number, the large-scale field strength decreases significantly. We found no significant quenching of the convective flows by the SSD, as recently claimed by other authors; in contrast, the convective flows first grow and then saturate for increasing Reynolds numbers. Furthermore, the angular momentum transport is highly affected by the presence of small-scale magnetic fields, which are mostly generated by tangling of the LSD. These fields not only change the Reynolds stresses, but also generate dynamically important Maxwell stresses. The LSD evolution in terms of its pattern and field distribution is rather independent of the increase in the fluid and magnetic Reynolds numbers.

**Conclusions.** At high fluid and magnetic Reynolds numbers, an SSD can be excited in addition to the LSD, and both strongly affect the angular momentum transport. Hence, it is important to study both dynamos and their interplay together to fully understand the dynamics of the Sun and other stars.

**Key words.** dynamo – magnetic fields – magnetohydrodynamics (MHD) – turbulence – Sun: magnetic fields – stars: activity

## 1. Introduction

The Sun and other cool stars exhibit large-scale magnetic fields that in some cases show cyclic variations (e.g. Baliunas et al. 1995; Boro Saikia et al. 2018; Olsper et al. 2018). This is associated with a large-scale dynamo (LSD) that operates in the stellar convection zones and produces complex magnetic features on the surface (Charbonneau 2014). In addition to the LSD, a small-scale dynamo (SSD) has been proposed to be present in these stars (e.g. Rempel et al. 2023). In contrast to an LSD, the SSD needs no large-scale rotation, shear, or stratification to operate, and the scales of its magnetic field are at or below the characteristic scales of the flow (Brandenburg & Subramanian 2005). There is some debate whether an SSD can operate in solar-like stars. These doubts were supported on one hand by numerical simulations, which showed that an SSD is increasingly harder to excite when approaching the solar param-

eters (Schekochihin et al. 2005), and on the other hand by the inconclusive results of small-scale field observations on the Sun (Bellot Rubio & Orozco Suárez 2019). Some observational studies showed a cyclic modulation of the internetwork field, that is, a connection to the cyclic large-scale magnetic field, whereas other studies showed that these fields are rather cycle-independent. The doubts based on numerical simulations, however, were recently alleviated by high-resolution simulations at magnetic Prandtl numbers ( $Pr_M$ ) that approached the solar value more closely than ever before (Warnecke et al. 2023). These simulations showed that an SSD is not only possible at these very low  $Pr_M$ , but that it becomes even easier to excite in this limit. This indicates a possible dynamical importance of the SSD in the Sun and solar-like stars.

The influence of SSD on the dynamics and LSD was studied with simplified setups (Vainshtein & Cattaneo 1992; Tobias & Cattaneo 2013; Squire & Bhattacharjee 2015; Singh et al. 2017; Väisälä et al. 2021), but global convective dynamo simulations (Käpylä et al. 2023) were only recently able to reach the regime in which both LSD and SSD are excited

\* Corresponding author; jorn.warnecke@aalto.fi, warnecke@mps.mpg.de



and can therefore be studied together (Hotta et al. 2016, 2022; Käpylä et al. 2017a; Hotta & Kusano 2021, hereafter HK21, HKS22). Hotta et al. (2016) reported that the SSD suppresses small-scale flows, which mimics the properties of an enhanced magnetic diffusivity. This in turn enhances the LSD. Käpylä et al. (2017a) found on the other hand that the SSD quenches differential rotation. Because this is one of the main dynamo drivers, it consequently suppressed the LSD in some of their cases.

The influence of the magnetic field on the differential rotation has been investigated in many previous analytical and numerical studies. The early global magnetoconvection studies of Gilman (1983) already showed that large-scale magnetism quenched differential rotation, but did not affect the convective motions in a clear manner. Analytical studies in the mean-field ( $\Lambda$  effect) framework produced similar results (e.g. Kitchatinov et al. 1994a). Many other global magnetoconvection studies followed (e.g. Fan & Fang 2014; Karak et al. 2015; Käpylä et al. 2016, 2023; Warnecke et al. 2013, 2016; Brun et al. 2022), but the most relevant for our work is Käpylä et al. (2017a), because it entailed an SSD. These authors reported that an increase in the magnetic Reynolds number  $\text{Re}_M$  leads to a strong suppression of differential rotation. The authors further suggested that the Maxwell stresses become comparable to the Reynolds stresses, and that therefore, only a weak differential rotation can be generated. They found that the increase in Maxwell stresses is partly due to a strong SSD. HK21 and HKS22 reported that the efficient SSD in their simulation was able to reshape an antisolar differential rotation into a solar one for increasing Reynolds numbers  $\text{Re}$ . Because the results obtained with different approaches diverge quite significantly, it is necessary to further investigate the role of SSD in LSD-active and differentially rotating systems. As magnetic fluctuations originate from different sources, namely SSD-action itself and tangling of the mean field through convective turbulence, it is also important to gain further insights into the role of these two contributions separately. These are the most important goals of this paper.

Since the pioneering work of Brandenburg (2016) and Käpylä et al. (2017b), it has been known that a more realistic description of the radiative heat diffusivity using the Kramers-opacity-based term can lead to the formation of subadiabatic layers at the base of the convection zone (e.g. Käpylä et al. 2019; Viviani & Käpylä 2021). The dependence of the shape and depth of these layers on  $\text{Re}$  or the presence of SSD and LSD has only been studied in a few Cartesian simulations (Hotta 2017; Käpylä 2019a, 2021), but not in a global setup.

We present a study of a global convective dynamo model in an azimuthal wedge of a spherical shell using the Kramers-opacity-based heat conductivity. We increased the resolution systematically from  $128 \times 256 \times 128$  to  $2048 \times 4096 \times 2048$  grid points to reach  $\text{Re}$  and  $\text{Re}_M$  of above 500. This parameter regime allowed us to investigate the LSD and SSD interaction in detail. To separately study the effect of the LSD and SSD on the overall dynamics, we ran for each configuration a full model, in which potentially both LSD and SSD can be excited; a reduced model, in which the large-scale field was removed to allow only for an SSD; and a hydrodynamic model without a magnetic field. The paper is organized as follows: In Sect. 2 we present our model and setup, in Sect. 3 we discuss the results in detail, and in Sect. 4 we present our conclusions. Additional information is given in Appendices A–C.

## 2. Model and setup

The stellar convection zone was modeled in spherical geometry  $(r, \theta, \phi)$  as a shell with a depth  $D = 0.3R$  similar to that in the Sun ( $0.7R \leq r \leq R$ ), where  $R$  is the radius of the star. We left

out the poles ( $\theta_0 \leq \theta \leq \pi - \theta_0$  with  $\theta_0 = 15^\circ$ ) and restricted our model to a quarter of the sphere (a wedge, with  $0 \leq \phi \leq \pi/2$ ), both for numerical reasons. Our model is similar to the models of Käpylä et al. (2013, 2016, 2019) and we refer to these papers for a detailed description.

We solved the fully compressible MHD equations in terms of the vector potential  $\mathbf{A}$  (ensuring the solenoidality of  $\mathbf{B}$ ), the velocity  $\mathbf{u}$ , the specific entropy  $s$ , and the density  $\rho$ , and we employed an ideal-gas equation of state. We included the rotational effects by adding the Coriolis force  $2\mathbf{u} \times \boldsymbol{\Omega}_0$  to the momentum equation, where  $\boldsymbol{\Omega}_0 = \Omega_0(\cos \theta, -\sin \theta, 0)$ , and  $\Omega_0$  is the angular velocity of the corotating frame of the modeled star, in which the plasma has zero total angular momentum. We chose a constant magnetic diffusivity  $\eta$  and kinematic viscosity  $\nu$ , except near the latitudinal boundaries, where we added  $\nu$  and  $\eta$  profiles in some of the runs for numerical reasons. These two profiles increased with  $\theta$  toward the boundaries across an interval  $\Delta\theta$  (see Appendix A for details). In our model, the diffusive heat flux has two contributions. The first contribution models the radiative heat flux as  $\mathbf{F}^{\text{rad}} = -K\nabla T$  with a temperature- and density-dependent radiative heat conductivity  $K$ , based on Kramers opacity, so that  $K$  is given by

$$K(\rho, T) = K_0 \left( \frac{\rho}{\rho_0} \right)^{-2} \left( \frac{T}{T_0} \right)^{13/2}, \quad (1)$$

and the reference values  $\rho_0$  and  $T_0$  were set to the corresponding values at the bottom of the domain in the initial (hydrostatic) state (for details, see Baretat & Brandenburg 2014; Käpylä et al. 2019; Viviani & Käpylä 2021). The second contribution mimics the heat flux of the unresolved or subgrid-scale (SGS) convection and stabilizes the system. This SGS heat flux is given by  $\mathbf{F}^{\text{SGS}} = -\chi_{\text{SGS}} \rho T \nabla s$ . As in Käpylä et al. (2013),  $\chi_{\text{SGS}}$  followed a smooth radial profile that was zero at the bottom of the domain, constant ( $\chi_{\text{SGS}} = \chi_{\text{m}}^{\text{SGS}}$ ) in the bulk, and maximum near the top, where it transports most of the heat. For some of the hydrodynamic runs, we needed to add a slope-limited diffusion (SLD) that acted on density and velocity to stabilize the system (see Appendix B for details).

The plasma was heated at the bottom by a constant heat flux and cooled at the top by blackbody radiation. The velocity  $\mathbf{u}$  was stress-free at all radial and latitudinal boundaries, and the entropy  $s$  had zero derivatives at the latitudinal boundaries. At the lower radial and at the latitudinal boundaries, we chose the magnetic field  $\mathbf{B}$  to follow a perfect conductor, while being purely radial at the top. In the  $\phi$  direction, the boundary conditions for all quantities were periodic.

Our runs were defined by the following nondimensional input parameters: We defined a normalized angular frequency and the Taylor number

$$\tilde{\Omega} = \Omega_0 / \Omega_\odot, \quad \text{Ta} = [2\Omega_0 D^2 / \nu]^2, \quad (2)$$

where  $\Omega_\odot = 2.7 \times 10^{-6} \text{ s}^{-1}$  is the rotation rate of the Sun, while the thermal, SGS-thermal, and magnetic Prandtl numbers were

$$\text{Pr} = \frac{\nu}{\chi_{\text{m}}}, \quad \text{Pr}_{\text{SGS}} = \frac{\nu}{\chi_{\text{m}}^{\text{SGS}}}, \quad \text{Pr}_{\text{M}} = \frac{\nu}{\eta}, \quad (3)$$

where  $\chi_{\text{m}} = K(r = r_{\text{m}}) / \rho c_{\text{p}}$  is the thermal diffusivity based on the Kramers opacity in the middle of the convection zone ( $r = r_{\text{m}}$ ), see Eq. (1), and  $c_{\text{p}}$  is the specific heat capacity at constant pressure. As  $K$  depends on local density and temperature, we used a one-dimensional hydrostatic model to determine  $K$

**Table 1.** Summary of runs.

Run	Resolution	Ta[10 <sup>8</sup> ]	$\overline{\text{Ra}}_{\text{Kram}}[10^7]$	$\overline{\text{Ra}}_{\text{SGS}}[10^7]$	$\widetilde{\text{Ra}}_{\text{SGS}}$	Pr	Re	Co	SLD	$\Delta\theta_v$	$\Delta\theta_\eta$	$\Delta_{v\eta}$
0M	128 × 256 × 128	1.25	73	1.2	48	5.13	27	10.4				
0H	128 × 256 × 128	1.25	73	1.2	48	5.13	28	9.9	Yes			
1M	256 × 512 × 256	5.00	280	5.9	94	1.52	61	9.3		5°	5°	2
1H	256 × 512 × 256	5.00	280	5.9	94	1.52	66	8.5	Yes			
2M	512 × 1024 × 512	20.0	1050	23.7	149	0.58	127	8.9		5°	5°	5
2S	512 × 1024 × 512	20.0	1050	23.7	149	0.58	139	8.1		5°	5°	5
2H	512 × 1024 × 512	20.0	1050	23.7	149	0.58	143	7.9	Yes	5°		5
3M	1024 × 2048 × 1024	80.0	3155	71.5	178	0.27	255	8.9		17°	17°	5
3S	1024 × 2048 × 1024	80.0	3155	71.5	178	0.27	265	8.5		17°	5°	5
3H	1024 × 2048 × 1024	80.0	3155	71.5	178	0.27	287	7.9	Yes	17°		5
4M	2048 × 4096 × 2048	320.0	7536	185.9	184	0.12	517	8.7		17°	5°	5
4M2	2048 × 4096 × 2048	320.0	7536	185.9	184	0.12	549	8.5		17°	5°	5
4S	2048 × 4096 × 2048	320.0	7536	185.9	184	0.12	550	8.2		17°	5°	5

**Notes.** Columns 2 to 7: input parameters. Columns 8 and 9: solution parameters, calculated from the saturated stage of the simulations. The last four columns indicate whether SLD and/or a diffusion profile in  $\theta$  was used with the corresponding parameters (see Appendices A and B). All runs had a density contrast  $\Gamma_\rho \equiv \langle \rho \rangle_{\theta\phi}(0.7R)/\langle \rho \rangle_{\theta\phi}(R)$  of roughly 30, and  $\tilde{\Omega} = 5$ ,  $\text{Pr}_{\text{SGS}} = 1$ . The M and S runs had  $\text{Pr}_M = 1$ .

and  $\rho$  for Pr. We note that Pr in the saturated stage can be significantly different from the hydrostatic model. Additionally, we defined two Rayleigh numbers calculated from the same hydrostatic model, one based on the Kramers heat diffusivity  $\chi$ ,

$$\text{Ra}_{\text{Kram}}(r) = \frac{GMD^4}{\nu\chi(r)R^2} \left( -\frac{1}{c_p} \frac{ds_{\text{hs}}}{dr} \right), \quad (4)$$

and the other on the SGS heat diffusivity  $\chi_{\text{SGS}}$ ,

$$\text{Ra}_{\text{SGS}}(r) = \frac{GMD^4}{\nu\chi_{\text{SGS}}(r)R^2} \left( -\frac{1}{c_p} \frac{ds_{\text{hs}}}{dr} \right), \quad (5)$$

where  $s_{\text{hs}}$  is the specific entropy in the hydrostatic model,  $G$  is the gravitational constant, and  $M$  is the total mass of the star. Our specific choices of Ra reflect the difficulty of defining a meaningful value for fully compressible convection. To meet the requirement of being determined by input parameters, that is, in the absence of convection, we used a one-dimensional version of our setup and allowed it to equilibrate to the hydrostatic state  $s_{\text{hs}}$ . As the Rayleigh numbers strongly depend on  $r$  and are not always positive in the middle of the domain (as in the non-Kramers runs), we averaged them over their logarithmized positive contribution  $\ln \text{Ra}_+$ ,

$$\overline{\text{Ra}} = \exp \langle \ln \text{Ra}_+(r) \rangle_r, \quad (6)$$

where the subscript  $r$  marks radial averaging.

To estimate the supercriticality, we defined a further Rayleigh number, in which the reduction of supercriticality due to rotation was compensated for by the Taylor number  $\widetilde{\text{Ra}} = \overline{\text{Ra}}/\text{Ta}^{2/3}$ , following (e.g. Chandrasekhar 1961; Roberts 1968; Barik et al. 2023).

We further characterized our simulations by the fluid and magnetic Reynolds numbers together with the Coriolis number,

$$\text{Re} = \frac{u_{\text{rms}}}{\nu k_f}, \quad \text{Re}_M = \frac{u_{\text{rms}}}{\eta k_f}, \quad \text{Co} = \frac{2\Omega_0}{u_{\text{rms}} k_f}, \quad (7)$$

where  $k_f = 2\pi/D \approx 21/R$  is an estimate of the wavenumber of the largest eddies in the domain, and  $u_{\text{rms}} = \sqrt{(3/2)\langle u_r^2 + u_\theta^2 \rangle_{r\theta\phi t}}$  is the rms velocity; the subscripts indicate averaging over  $r, \theta, \phi$ ,

and a time interval covering the saturated state. This definition is a good estimate of the turbulent velocity because the meridional circulation is weak in all of our runs and the 3/2 factor accounts for the omitted azimuthal component of  $\mathbf{u}$  (see also Käpylä et al. 2013 for more details).

The nondimensional input and solution parameters are given in Table 1 for all runs. In summary, we used the same model as in Käpylä et al. (2016), except that we applied the Kramers heat conductivity instead of a fixed conductivity profile.

For our analysis throughout the paper, we decomposed each field into a mean (axisymmetric) and a fluctuating part, which are indicated by an overbar and a prime, respectively. For example,  $\mathbf{B} = \overline{\mathbf{B}} + \mathbf{B}'$  and  $\mathbf{u} = \overline{\mathbf{u}} + \mathbf{u}'$ . Restricted to fluctuating fields, we defined an  $r$ - and  $\theta$ -dependent turbulent rms velocity  $u'_{\text{rms}}(r, \theta) = \langle \overline{\mathbf{u}'^2} \rangle_t^{1/2}$ , turbulent rms magnetic field strength  $B'_{\text{rms}}(r, \theta) = \langle \overline{\mathbf{B}'^2} \rangle_t^{1/2}$ , and turbulent equipartition field strength  $B_{\text{eq}}(r, \theta) = u'_{\text{rms}}(\mu_0 \overline{\rho})^{1/2}$ , where  $\mu_0$  is the magnetic vacuum permeability. The total kinetic energy density is defined as

$$E_{\text{kin}}^{\text{tot}} = \frac{1}{2} \langle \rho \mathbf{u}^2 \rangle_V, \quad (8)$$

which is further decomposed into the energy densities of the fluctuating velocity, the differential rotation, and the meridional circulation,

$$E_{\text{kin}}^{\text{flu}} = \frac{1}{2} \langle \rho \mathbf{u}'^2 \rangle_V, \quad E_{\text{kin}}^{\text{dif}} = \frac{1}{2} \langle \rho \overline{u_\phi^2} \rangle_V, \quad E_{\text{kin}}^{\text{mer}} = \frac{1}{2} \langle \rho (\overline{u_r^2} + \overline{u_\theta^2}) \rangle_V. \quad (9)$$

Here,  $\langle \cdot \rangle_V$  indicates volume averaging. In a similar way, the total magnetic energy density is defined as

$$E_{\text{mag}}^{\text{tot}} = \frac{1}{2\mu_0} \langle \mathbf{B}^2 \rangle_V, \quad (10)$$

and it can be split into the energy density of the fluctuating field, along with those of the toroidal and poloidal mean fields,

$$E_{\text{mag}}^{\text{flu}} = \frac{1}{2\mu_0} \langle \mathbf{B}'^2 \rangle_V, \quad E_{\text{mag}}^{\text{tor}} = \frac{1}{2\mu_0} \langle \overline{B_\phi^2} \rangle_V, \quad E_{\text{mag}}^{\text{pol}} = \frac{1}{2\mu_0} \langle \overline{B_r^2} + \overline{B_\theta^2} \rangle_V. \quad (11)$$

The presented analyses and quantities were performed and calculated from the saturated stage of the simulations. The

rescaling to physical units was based on the solar rotation rate  $\Omega_\odot = 2.7 \times 10^{-6} \text{ s}^{-1}$ , solar radius  $R = 7 \times 10^8 \text{ m}$ , density at the bottom of the domain  $\rho(0.7R) = 200 \text{ kg/m}^3$ , and  $\mu_0 = 4\pi \cdot 10^{-7} \text{ H m}^{-1}$ . As discussed in Käpylä et al. (2013, 2014), this is one particular choice that gives meaningful results for the input flux, the velocities, and magnetic field strengths in the bulk of the convection zone. All simulations were performed using the PENCIL CODE (Pencil Code Collaboration 2021).

### 3. Results

Our goal was to study the LSD and SSD together in a setup that includes a physically motivated heat conductivity based on the Kramers opacity. As our starting point, we used the model of Käpylä et al. (2016), with the only difference that we replaced the prescribed heat conductivity by a conductivity based on the Kramers opacity; this represents Run 0M. We then lowered step by step the viscosity  $\nu$ , the magnetic diffusivity  $\eta$ , and the SGS heat diffusivity  $\chi_{\text{SGS}}$ , which caused the simulation to become gradually more turbulent, while keeping  $\text{Pr}_{\text{SGS}}$  and  $\text{Pr}_M$  constant. At each step, indicated by the number in the run label, the diffusivities were halved, which led to a total reduction by a factor of 16 from Set 0 to Set 4. Technically, this required doubling the resolution and remeshing the run at each step, and finally, running the simulation in the saturation regime for a sufficient time span.

To study the effects of the SSD in isolation and to determine whether it was indeed present, we forked each MHD run into two with identical setups: In the first setup, denoted with S, we removed the mean field  $\bar{\mathbf{B}}$  at every fifth<sup>1</sup> time step. No LSD was therefore able to develop. When an SSD was sustained, we studied it in detail. In the second setup, denoted by M, we did not remove the mean field, and the LSD was therefore able to develop freely. Finally, we also performed the corresponding hydrodynamic simulations, denoted by H. Run 4M2 was basically the same as 4M, but we did not remesh and restart from 3M, which had an LSD, but restarted from 4S, where only an SSD was present. This again allowed the LSD to grow after the restart. Our motivation was here to study whether an LSD can be excited and grow in the presence of already existing strong magnetic fluctuations. Runs 0M to 2M were similar to Runs G1 to G3 in Käpylä et al. (2017a), whereupon the difference is in the use of the Kramers-opacity-based heat conductivity in our work and in a normal magnetic field condition at the latitudinal boundaries in G2 and G3.

All runs are listed in Table 1 with their control and solution parameters. We note that an SSD is present in Sets 2–4, implying that its critical  $\text{Re}_M$  lies between roughly 60 and 130. This is consistent with the study of Käpylä et al. (2017a), who typically found an SSD for  $\text{Re}_M > 60$ . Interestingly, run G2 of Käpylä et al. (2017a) has an SSD with  $\text{Re}_M = 66$ , in contrast to our Run 2M with  $\text{Re}_M = 61$ , which does not excite an SSD. Either the SSD is very close to critical, or the slight differences in the setups are causal. We note here that  $\text{Re}_M$  in their work and ours is only an average, and it hence does not reflect the detailed local dynamics. The critical  $\text{Re}_M$  we found is somewhat higher than what was obtained from theoretical models for smooth velocity fields at low compressibility, which yielded predictions of about 30–60 (Brandenburg & Subramanian 2005), and 30–50 for simple isothermal forced-turbulence models (e.g. Schekochihin et al. 2005; Väisälä et al. 2021; Warnecke et al. 2023).

When the diffusivities are decreased, the Rayleigh numbers  $\text{Ra}_{\text{Kram}}$  and  $\text{Ra}_{\text{SGS}}$  strongly increase by a factor of more than

<sup>1</sup> This cadence was chosen to avoid slowing down the computing while still removing the large-scale field efficiently.

100. However, because also the Taylor number,  $\text{Ta}$ , increases significantly by a factor of nearly 300, one needs to inspect the compensated Rayleigh number  $\widetilde{\text{Ra}}_{\text{SGS}}$  to assess whether the supercriticality increased as well. Indeed,  $\widetilde{\text{Ra}}_{\text{SGS}}$  is nearly four times higher in the run with the lowest diffusivities than in the run with the highest diffusivities. The rotational influence on the convection in terms of  $\text{Co}$  decreased only slightly when the diffusivities were decreased because the turbulent convection becomes slightly stronger.  $\text{Pr}$  is above unity for Sets 0 and 1 and below unity for Sets 2–4, indicating that heat conduction (in the middle of the convection zone) is dominated by the SGS contribution for Sets 0 and 1 and by the Kramers contribution otherwise. We recall, however, that these two terms involve different gradients.

All runs reached dynamical saturation in terms of their running time  $t_{\text{max}}$  being a multiple of the convective turnover time  $\tau = 1/u_{\text{rms}}k_f$ ; i.e.,  $t_{\text{max}}/\tau > 3000$  for Sets 0, 1 and 2,  $t_{\text{max}}/\tau > 360$  for Set 3, and  $t_{\text{max}}/\tau > 2.4$  for Set 4. In terms of the turbulent magnetic diffusion time  $\tau_{\text{mag}}^{\text{turb}} = D^2/\eta_t$  with  $\eta_t = u_{\text{rms}}k_f/3$ , which is important for the evolution of the mean field, all runs from Sets 0–3 reached multiples of  $\tau_{\text{mag}}^{\text{turb}}$  and hence can be considered to be in a steady state (see also the discussion in Sect. 3.2).

#### 3.1. Overview of the dynamics

As shown in Fig. 1 for all the M runs, the radial velocity becomes more turbulent and develops progressively more small-scale structures when the diffusivities are decreased and hence the Reynolds numbers increase. For all runs, prominent thermal Rossby waves, also known as Busse columns or banana cells (e.g. Busse 1970, 1976; Featherstone & Hindman 2016; Bekki et al. 2022), were present outside the tangent cylinder in the equatorial regions. This agrees with earlier models and theoretical expectations. Interestingly, the longitudinal degree of these waves did not vary much with increasing  $\text{Re}$ . It was mostly between  $m = 32$  and  $m = 40$  for all runs (see Appendix C for a more detailed analysis).

In Fig. 2 we show the corresponding radial magnetic field close to the surface for all the M runs. Near the equator, the radial magnetic field is mostly concentrated in the downflow lanes of the banana cells, where it forms complex structures with small bipolar patches. The radial field is mostly dominated by magnetic fluctuations, while the mean field is not visible near the equator. At higher latitudes in Runs 0M–2M, hints of longitudinal bands of the same polarity as traces of the weak mean radial field are visible. For 3M, 4M, and 4M2, these patterns are no longer as clearly visible.

In Fig. 3 we show the azimuthal magnetic field for Runs 2M, 2S, 3M, 3S, 4M, and 4S. For this component, the difference between Sets S and M is most pronounced. In the M runs, the mean field is clearly visible at all covered latitudes. The magnetic fluctuations in these runs are also present ubiquitously. In Run 2S, the fluctuating magnetic field is more concentrated near the equator. The fluctuations become distributed over progressively wider latitude ranges when the Reynolds numbers are increased (see Runs 3M to 4M). Interestingly, the banana-cell pattern does not produce a strong imprint on the azimuthal magnetic field structure.

#### 3.2. Energies

Next, we studied the total (volume-averaged) energy densities, as shown in Fig. 4 and Table 2. For the H runs, the kinetic energy is generally higher than for the other sets, and it is dominated by the



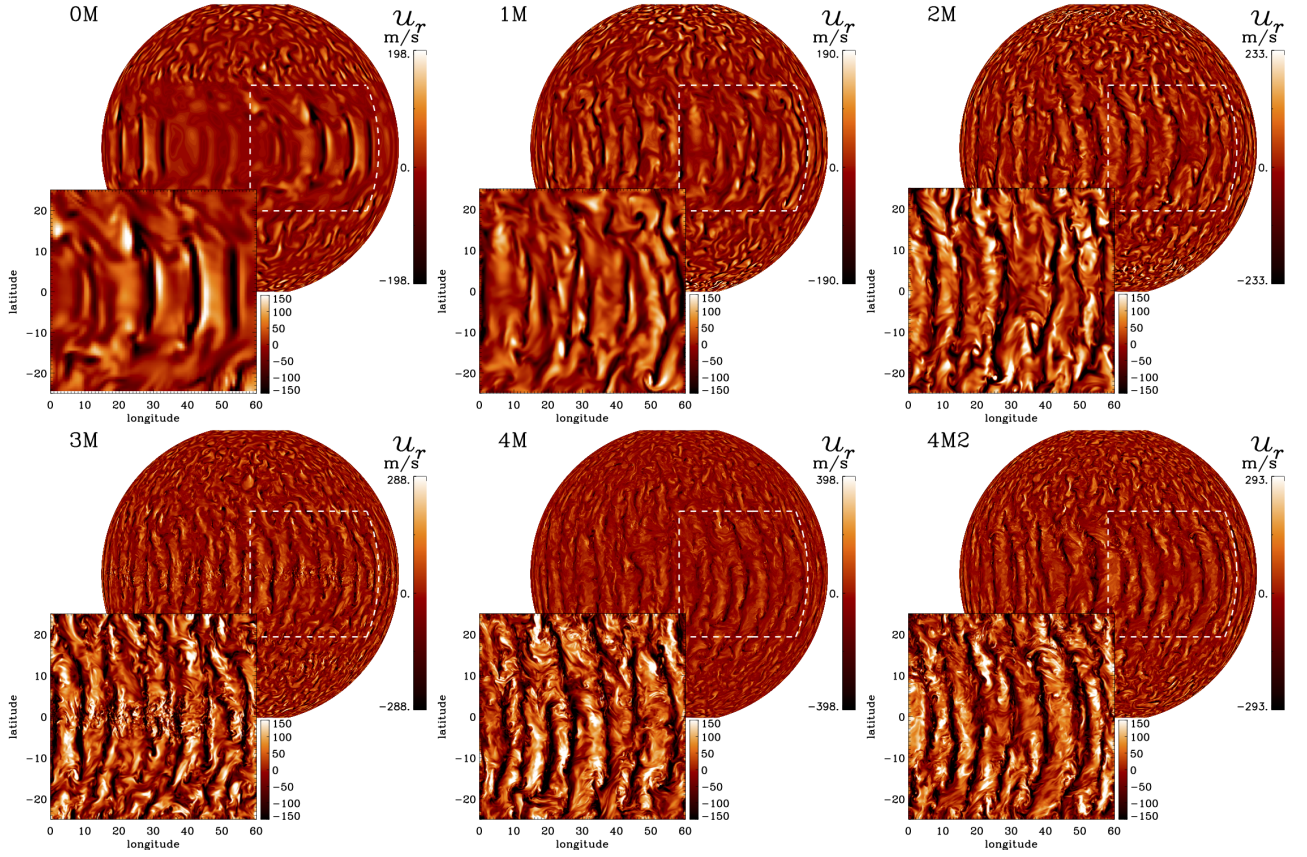


**Fig. 1.** Radial velocity  $u_r$  at  $r = 0.98 R$  with a low-latitude cutout for all M runs in the saturated stage. The wedge is duplicated to form a half-sphere.

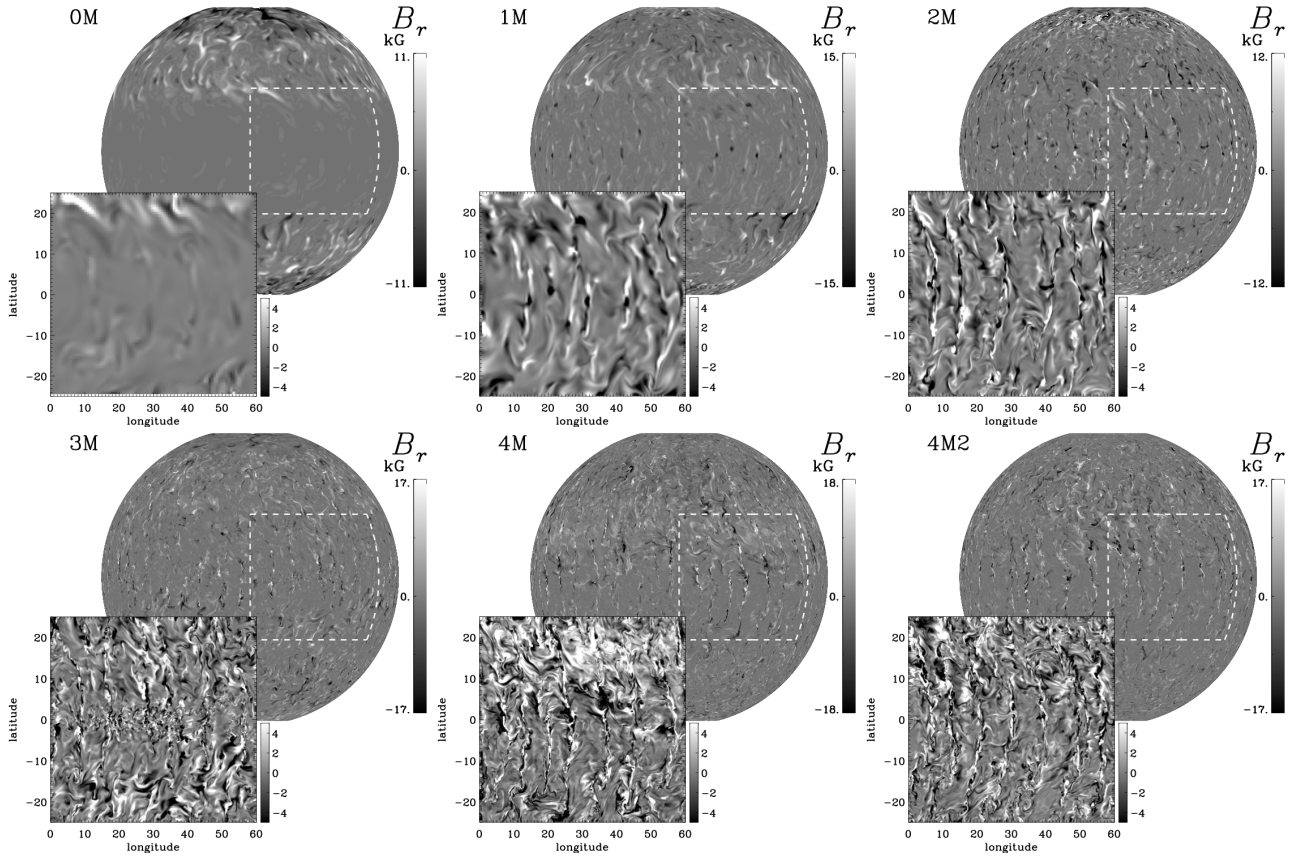


**Fig. 2.** Radial magnetic field  $B_r$  at  $r = 0.98 R$  for all M runs. Otherwise the same as Fig. 1.



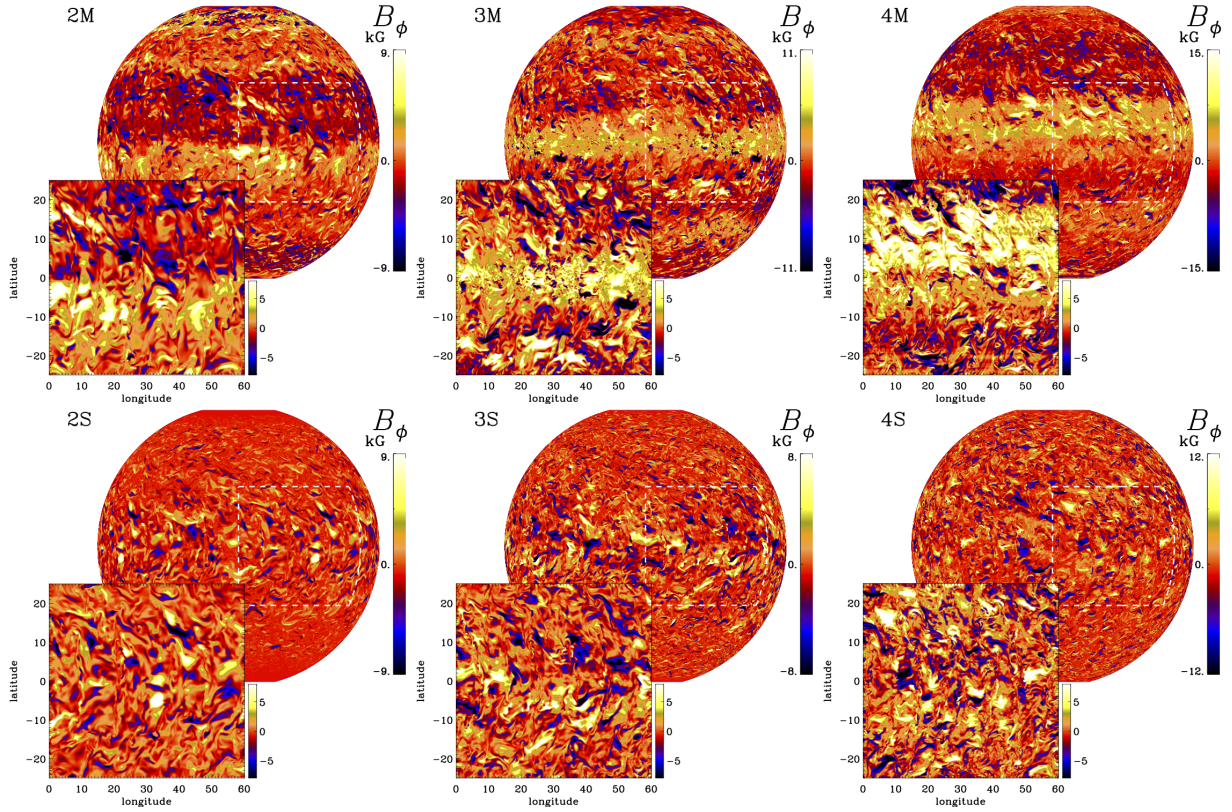


**Fig. 3.** Azimuthal magnetic field  $B_\phi$  at  $r = 0.98 R$  for all M runs with an SSD and the corresponding S runs. Otherwise the same as Fig. 1.

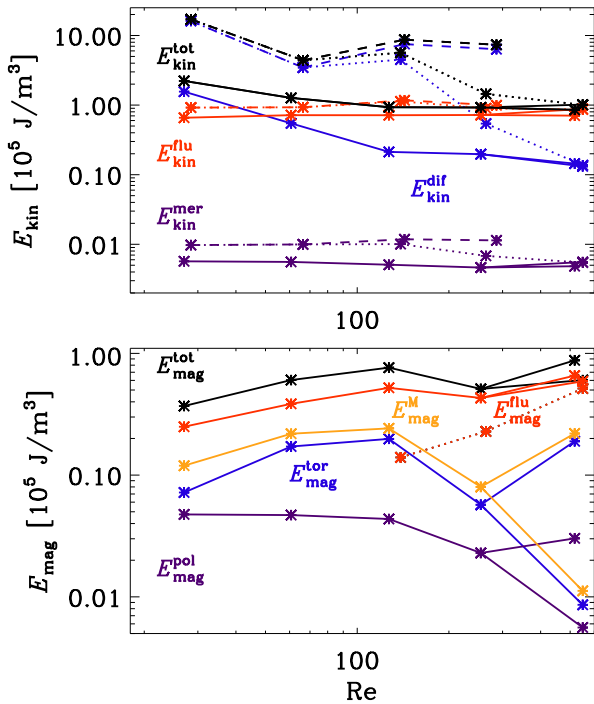


**Fig. 4.** Dependence of the kinetic and magnetic energy densities on  $Re$ . In the top panel, we show  $E_{kin}^{tot}$  (black), which is composed of  $E_{kin}^{flu}$  (red),  $E_{kin}^{dif}$  (blue), and  $E_{kin}^{mer}$  (purple) for H runs (dashed), M runs (solid), and S runs (dotted). In the bottom panel, we show  $E_{mag}^{tot}$  (black) composed of  $E_{mag}^{flu}$  (red),  $E_{mag}^{tor}$  (blue), and  $E_{mag}^{pol}$  (purple).  $E_{mag}^{tot} = E_{mag}^{tor} + E_{mag}^{pol}$  is the energy density of the mean magnetic field (yellow) (see Eqs. (8)–(11) for definitions). The lower mean-field energy densities for  $Re \sim 530$  indicate Run 4M2, which has been started from Run S4 and is possibly not yet saturated, hence the bifurcation.

differential rotation at all  $Re$ . For the M runs, the contribution of the differential rotation becomes weaker and subdominant with respect to the velocity fluctuations with increasing  $Re$ . For the lowest considered diffusivities, however, the contribution of the differential rotation to the total kinetic energy seems to level off at a value of roughly 15%. The contribution of the meridional circulation is tiny for all runs. The energies of the fluctuating velocities remain for roughly constant at increasing  $Re$ , for all sets, but are slightly higher for the H runs than for the M runs.

The S runs with small  $Re$  show a similar dominance of differential rotation, but its contribution diminishes for growing  $Re$ , similarly to the M runs. The S runs basically show a transition from an almost purely hydrodynamic state (2S) to a fully magnetically dominated state (4S). This has to be attributed to the SSD, which strongly increases with growing Reynolds numbers, as we discuss below.

The magnetic energy increases with increasing  $Re$  for the first three M runs. This is mostly due to the increase in the mean field. For higher  $Re$ , the energy in the mean field actually decreases, whereas the contribution of the small-scale field increases. The results for the lowest diffusivities (4M, 4M2) need to be taken with caution: Run 4M was restarted from a remeshed earlier stage of 3M, at which the mean-field energy was still high (see Fig. 13 and its discussion in Sect. 3.6). Run 4M2 was started from 4S to determine how fast the mean field was able to recover after it was removed. After running for  $\sim 0.06$  yr, the mean field was still very weak.

For all runs, the mean field is dominated by its toroidal part. For all M runs, the small-scale field contribution dominates the total magnetic energy and shows some tendency to increase for high  $Re$ . In the runs without SSD (0M and 1M), the fluctuations

**Table 2.** Energy densities for all runs.

Run	$E_{\text{kin}}^{\text{tot}}$	$E_{\text{kin}}^{\text{dif}}$	$E_{\text{kin}}^{\text{mer}}$	$E_{\text{kin}}^{\text{flu}}$	$E_{\text{mag}}^{\text{tot}}$	$E_{\text{mag}}^{\text{tor}}$	$E_{\text{mag}}^{\text{pol}}$	$E_{\text{mag}}^{\text{flu}}$	$E_{\text{mag}}^{\text{tot}}/E_{\text{kin}}^{\text{tot}}$	$E_{\text{mag}}^{\text{flu}}/E_{\text{kin}}^{\text{flu}}$
0M	2.225	1.562	0.006	0.658	0.369	0.072	0.048	0.250	0.166	0.379
0H	17.089	16.159	0.010	0.920						
1M	1.267	0.546	0.006	0.716	0.604	0.172	0.047	0.385	0.476	0.538
1H	4.397	3.457	0.010	0.930						
2M	0.933	0.213	0.005	0.715	0.763	0.198	0.044	0.521	0.819	0.729
2S	5.643	4.503	0.010	1.130	0.140	0.000	0.000	0.140	0.025	0.124
2H	8.697	7.514	0.012	1.171						
3M	0.923	0.197	0.005	0.721	0.510	0.057	0.023	0.430	0.553	0.597
3S	1.448	0.542	0.007	0.900	0.228	0.000	0.000	0.228	0.158	0.254
3H	7.352	6.347	0.011	0.993						
4M	0.854	0.144	0.005	0.705	0.876	0.190	0.030	0.656	1.026	0.931
4M2	1.016	0.132	0.006	0.879	0.604	0.009	0.006	0.590	0.594	0.671
4S	1.004	0.137	0.005	0.862	0.514	0.000	0.000	0.515	0.512	0.597

**Notes.** The energy densities (Cols. 2 to 9) are in  $10^5 \text{ J/m}^3$ , for their definitions see Eqs. (8)–(11).

contribute roughly 65% to the total magnetic energy. When the SSD starts operating, this contribution increases from 68% (Run 2M) to 75% (4M).

In the S runs, we observe a significant increase in the magnitude of the magnetic fluctuations due to the strengthening SSD. Let us assume that  $E_{\text{mag}}^{\text{flu}}$  in the S runs represents the strength of the SSD-generated field well also in the corresponding M runs, despite some differences in the flow dynamics. For  $\text{Re} \sim 130$ , a quarter of  $E_{\text{mag}}^{\text{flu}}$  is then due to the SSD, which increases to nearly 80% for  $\text{Re} \sim 500$ .

In our interpretation, the quenching of the differential rotation at low  $\text{Re}$  is caused by the small-scale field that is generated by the tangling of the large-scale magnetic field and not directly by the large-scale field. At higher  $\text{Re}$ , the SSD also generates a small-scale field, which further quenches the differential rotation.

Disregarding Run 4M because of the issues mentioned above, the total magnetic field energy tends to saturate at high  $\text{Re}_M$  because the increase in the fluctuating-field energy compensates for the decrease in the mean-field magnetic energy. This is in contrast to previous studies (Nelson et al. 2013; Hotta et al. 2016; Käpylä et al. 2017a), where the total field increased monotonically with  $\text{Re}_M$ . However, for the mean field, our study is roughly consistent with the results of Nelson et al. (2013) and Hotta et al. (2016). These authors reported that the mean-field energy decreased with  $\text{Re}_M$ . Our study is inconsistent with our previous work (Käpylä et al. 2017a), however, where the mean field did not decrease.

The total magnetic energy is close to equipartition with the total kinetic energy only at the highest  $\text{Re}$  (4M) because of the strong mean field and its tangled fluctuating field (see the last two columns of Table 2). In the pure SSD runs, the field reached only 50% of the equipartition value. This disagrees with the results of HKS22, who found superequipartition fields at their highest resolution. The comparison with recent work by Yan & Calkins (2022) on large- and small-scale convective dynamics in plane layers yields several differences: They reported that the ratio of the magnetic to kinetic energy decreased with increasing  $\widetilde{\text{Ra}}$ , but showed some tendency to saturate from  $\widetilde{\text{Ra}} \approx 50$  on. In contrast, we found the opposite trend, but in the  $\widetilde{\text{Ra}}$  interval [48, 184]. Moreover, we cannot confirm their conclusion that SSDs are likely to yield lower energy ratios. We recall, however, that their simulations were performed at  $\widetilde{\text{Re}}_M \text{Ta}^{1/6} \approx O(1)$ , whereas we covered the  $\widetilde{\text{Re}}_M$  interval [26, 210].

### 3.3. Overshoot and Deardorff layers

Similar as in the work of Käpylä et al. (2019) and Viviani & Käpylä (2021), we found that using a Kramers-based heat conductivity causes the development of subadiabatic but convective layers in addition to the usual convective zone. From top to bottom of the domain, the zones are defined as

$$\overline{F}_{\text{enth}} > 0, \quad ds/dr < 0 \quad \text{buoyancy zone (BZ)} \quad (12)$$

$$\overline{F}_{\text{enth}} > 0, \quad ds/dr > 0 \quad \text{Deardorff zone (DZ)} \quad (13)$$

$$\overline{F}_{\text{enth}} < 0, \quad ds/dr > 0 \quad \text{overshoot zone (OZ)} \quad (14)$$

$$\overline{F}_{\text{enth}} < 0, \quad |\overline{F}_{\text{enth}}| < 0.03 \overline{F}_{\text{tot}} \quad \text{radiative zone (RZ)}, \quad (15)$$

where  $\overline{F}_{\text{enth}} = c_p \overline{(\rho u_r)' T'}$  is the radial enthalpy flux, and  $\overline{F}_{\text{tot}} = \overline{F}^{\text{rad}}(0.7R)$  is the total flux, defined by the flux through the bottom boundary. In the definitions above, all fluxes are additionally averaged over latitude, and hence, they only depend on the radius  $r$ .

We investigate the dependence of these zones on  $\text{Re}$  for different runs in Fig. 5. As a first result, we observe that approximately the lower quarter of the domain is convectively stable (even more so for low  $\text{Re}$ ). This is consistent with previous works in similar parameter regimes (Käpylä et al. 2019; Viviani & Käpylä 2021).

The DZ is more pronounced near the equator in the high-diffusivity runs, especially in hydro cases. As  $\text{Re}$  increases, the DZs become narrower near the equator and more uniform over latitude, while their radial extent at high latitudes depends on the presence of magnetic fields. In the M runs, the DZ becomes very thin and is partly replaced by a thin OZ and an extended RZ for high  $\text{Re}$ . In the S runs, the DZ is more pronounced at low latitudes, even at high  $\text{Re}$ . For the H runs, it is always pronounced at low latitudes. At high  $\text{Re}$ , however, most of it is replaced by the overshoot zone.

Regarding the discussion on the dependence of the OZ depth on  $\text{Re}$  (see Hotta 2017; Käpylä 2019a), our conclusion is complex. For all runs, the depth at high latitudes seems to remain rather constant, which agrees with Käpylä (2019a, 2021). At low latitudes, however, the depth decreases with  $\text{Re}$  for the H runs, which agrees with Hotta (2017), but it increases in the S runs. For the depth of the DZ, Käpylä (2021) reported a weak dependence



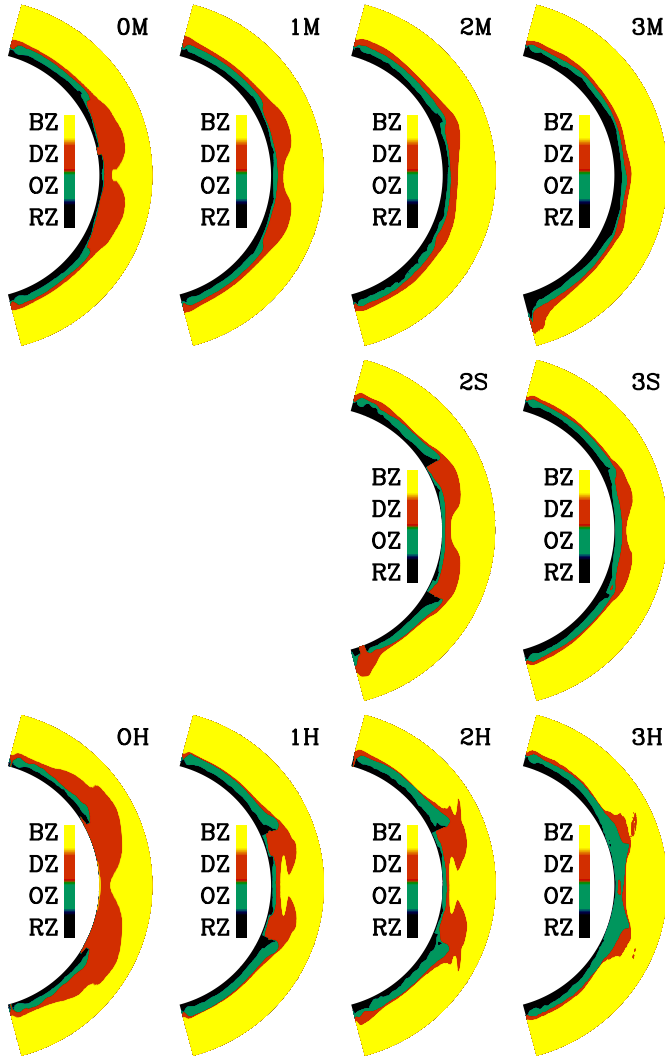


**Fig. 5.** Visualization of the four zones formed in the simulations: buoyancy (BZ, yellow), Deardorff (DZ, red), overshoot (OZ, green), and radiative zone (RZ, dark blue) (see Sect. 3.3 for definitions).

on  $Re$ , which we can confirm for high latitudes, but not throughout.

### 3.4. Flow and magnetic field distribution

The variation in the fluid and magnetic Reynolds numbers also impacts the distribution of the turbulent velocity and the magnetic fields. In Fig. 6 we illustrate the latitudinally averaged radial profiles of  $u'_{rms}$  for all runs and compare them with the values for the Sun, relying on the mixing-length theory (MLT) (see the green line for the Standard Solar Model of Table 6.1 in Stix 2002). As MLT provides only radial velocities, we multiplied them with  $\sqrt{3}$  to obtain an estimate of  $u_{rms}$  assuming isotropy of the flow. These values of the convective velocities need to be taken with caution as they rely on crucial assumptions, such as the value of the MLT parameter. Furthermore, helioseismic analysis has cast doubt on them (e.g. Hanasoge et al. 2012).

First, our values are somewhat lower than those from the Sun, which is expected because the rotational effects in our simulations are stronger, as indicated by the Coriolis numbers, which range from  $Co = 8$  to  $9$ . Near the surface, significant discrepancies arise that are likely due to the absence of a strong density

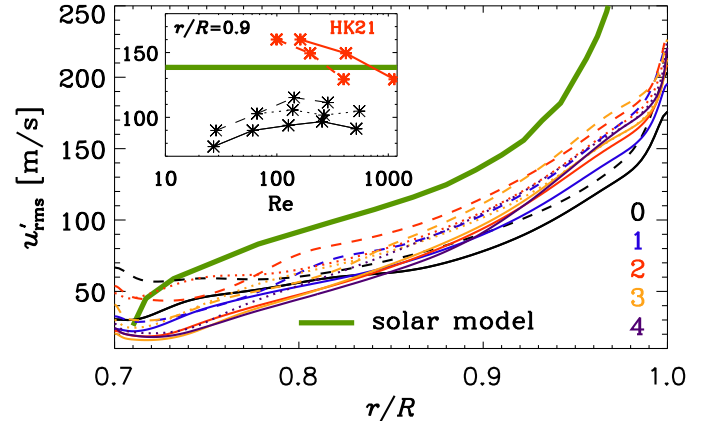


**Fig. 6.** Radial profile of the latitudinally averaged turbulent velocity  $u'_{rms}$  of all runs. The colors indicate the different run sets with different  $Re$  as indicated. The solid lines show M runs, the dotted lines show S runs and the dashed lines show H runs. The thick green line indicates the values from the solar model of Stix (2002) based on mixing-length theory. The inset shows  $u'_{rms}$  at a fixed radius  $r = 0.9R$  as a function of  $Re$ . There, we overplot  $u'_{rms}$  of Hotta & Kusano (2021) using the  $Re$  estimated in HKS22 (solid red) and a reestimate according to Eq. (16) (dashed).

stratification. The M runs show the poorest agreement, while the H runs exhibit higher velocities than their M counterparts. The S runs fall between these two. We interpret this as suppression of the turbulent velocities by magnetic fields, primarily by those that are generated by the large-scale dynamo.

Upon investigating the turbulent velocity as a function of  $Re$  at  $r = 0.9R$  (see inset in Fig. 6), we observed as before that for all H runs,  $u'_{rms}$  is larger than for the M runs, with the S runs consistently in between. The velocity fluctuations initially increased for all run sets with  $Re$  and then decreased for higher  $Re$ . This decrease is not as pronounced as the initial increase, however. The decrease in  $u'_{rms}$  in Run 4M might be caused by the magnetic field, but we observed a mild decrease in Run 3H as well and even an increase for Run 4S. Therefore, this interpretation may not be entirely valid.

We also compared our velocities to the results of HK21, who reported that the SSD suppressed the turbulent velocity as their effective  $Re$  increased. The authors did not explicitly define  $Re$  because they used a SLD scheme without explicit diffusivities, and they therefore estimated  $Re$  using the Taylor microscale. As an alternative, we estimated their  $Re$  using the grid spacing of our Set 4,

$$Re_{HK21} = Re_4 \Delta\phi_4 / \Delta\phi_{HK21}. \quad (16)$$

Here,  $Re_4 = 530$  is a rough average of all  $Re$  in Set 4,  $\Delta\phi_4 = \pi/2/2048$  is the grid size in this set, and  $\Delta\phi_{HK22} = 2\pi/(1536, 3072, 6144)$  is the variable grid size of the three runs of HK21. This approach ensured that  $Re$  did not increase much more than by a factor of two when the resolution was doubled, in contrast to the approach of HKS22.

The comparison revealed two significant findings: First, as evident from the inset of Fig. 6, their  $u'_{rms}$  values are markedly higher than ours and exceed those of the Standard Solar Model (Stix 2002) for their low and medium resolutions. Second, our simulations do not exhibit a decrease in  $u'_{rms}$  with increasing  $Re$ , as notable as observed in HK21. Instead, we only observe a mild decrease at high  $Re$ . Two explanations for this behavior can be considered: First, it may be linked to the more efficient SSD in the highest-resolution simulation of HK21, which is likely a

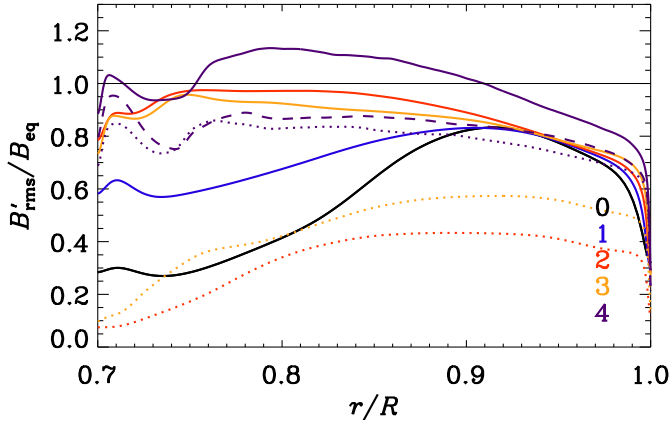


**Fig. 7.** Radial profile of the normalized latitudinally averaged turbulent magnetic field  $B'_{\text{rms}}/B_{\text{eq}}$  of all runs. The color-coding and line styles are the same as in Fig. 6, with the exception of Run 4M2 (purple dashed line).

result of higher turbulent velocities. Second, it might be a consequence of their use of a pure SLD scheme for viscous and magnetic diffusion, as opposed to the constant explicit diffusivities employed in our study. This is supported by the fact that HK21 achieved a more efficient SSD at an even lower resolution than we did.

However, if the turbulent velocities were quenched by the SSD at high Re, we would expect to see a suppression of  $u'_{\text{rms}}$  as a function of Re only for the M and S runs, but we also observe it for H runs. Another possible cause may be the specific setup of HK21, who fixed the energy fluxes to the solar luminosity at both radial boundaries, forcing the total energy to remain constant at its initial value. This constraint assumes that the initial stage is already very close to the final solution, because large departures from the initial stratification are not possible. This makes the solution intrinsically not self-consistent. We are confident that our model, which allows the thermal energy to adjust to the dynamics, is more self-consistent and hence more realistic.

Next, we examined the latitudinally averaged turbulent magnetic field strength  $B'_{\text{rms}}$ , normalized by the equipartition field strength in Fig. 7 (see Fig. 6 for the turbulent kinetic energy). As expected, the turbulent magnetic field increased with Re for the M and S runs. Weak superequipartition fields were only observed for Run 4M in the middle of the convection zone. Runs 4M2, 4S, 3M, and 2M reached values above  $B'_{\text{rms}}/B_{\text{eq}} = 0.9$ , but did not exceed unity in the entire convection zone. The pure SSD (S) runs consistently exhibited weaker  $B'_{\text{rms}}$  than their M counterparts.

Interestingly, the field increased with  $\text{Re} (= \text{Re}_M)$  for the M runs, mostly in the lower half of the convection zone, and it appeared to be mostly independent of  $\text{Re}_M$  in the upper part of the domain. Only the highest  $\text{Re}_M$  run (4M) showed a slightly enhanced field in the upper part of the domain. In contrast, the S runs showed an increase in  $B'_{\text{rms}}$  with  $\text{Re}_M$  throughout the domain. We interpret this as follows: In the M runs, where the SSD is still weak,  $B'_{\text{rms}}$  is primarily generated by the tangling of the large-scale magnetic field. This process seems independent of Re for the upper part of the domain but becomes more effective in the lower part of the domain as Re increases. As the SSD increases similarly at all radii, it also enhances  $B'_{\text{rms}}$  for the highest Re runs, where the SSD field becomes comparable to the tangled field.

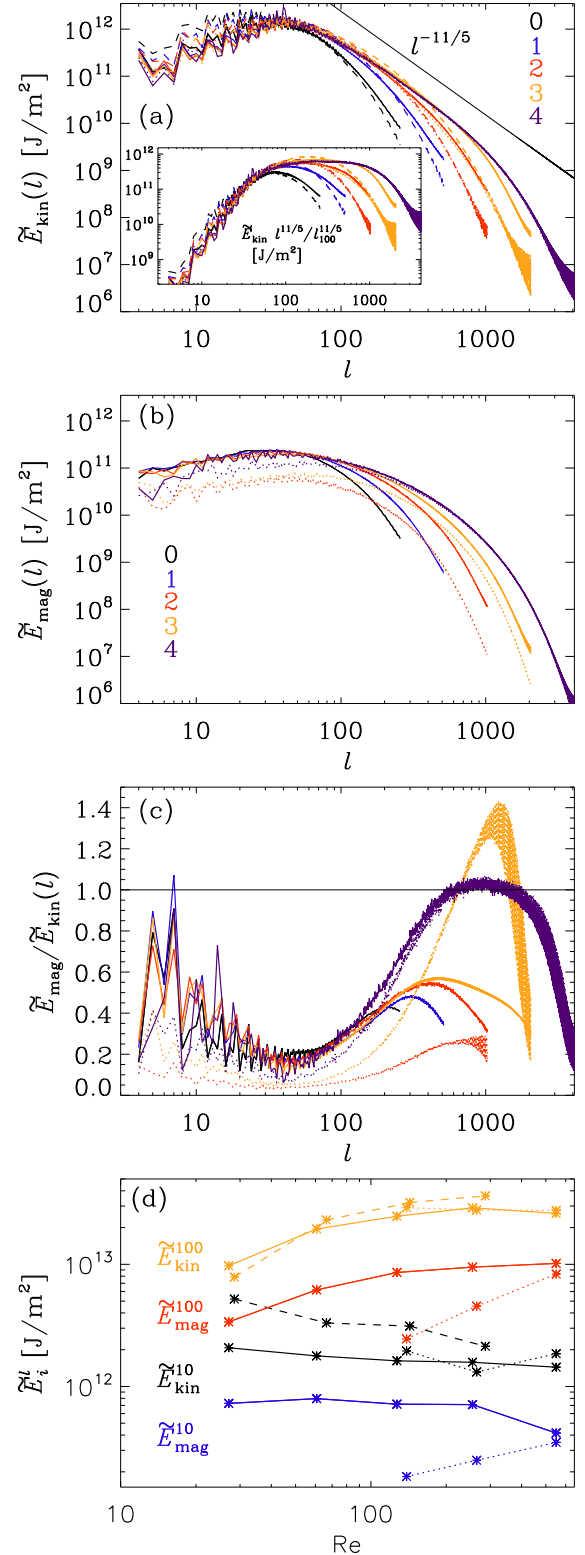


**Fig. 8.** Spectra of kinetic (a) and magnetic (b) energy density along with their ratio (c) near the surface,  $r = 0.98R$ , all excluding the  $m = 0$  contribution. As before the solid lines show M runs, the dotted lines show S runs and the dashed lines show H runs, while different colors indicate run sets with distinct Re. Panel (d) highlights the Re dependence of the kinetic and magnetic spectra for  $l = 10$  and  $100$ .

In Fig. 8 we present the spherical-harmonic spectra of kinematic and magnetic energies along with their ratio for all runs, calculated from near the surface ( $r = r_s \equiv 0.98R$ )  $\theta\phi$  slices. The

spectral energies  $\tilde{E}_{\text{kin}}(l)$  and  $\tilde{E}_{\text{mag}}(l)$  were calculated using the following definitions:

$$\sum_l \tilde{E}_{\text{kin}}(l) = r_s E_{\text{kin}}|_{r=r_s} \quad \sum_l \tilde{E}_{\text{mag}}(l) = r_s E_{\text{mag}}|_{r=r_s}, \quad (17)$$

where  $l$  is the spherical-harmonic degree, and the energy densities are given as

$$E_{\text{kin}}|_{r=r_s} = \frac{1}{2\mu_0} \langle \rho \mathbf{u}'^2 \rangle_{\theta\phi}|_{r=r_s} \quad E_{\text{mag}}|_{r=r_s} = \frac{1}{2\mu_0} \langle \mathbf{b}'^2 \rangle_{\theta\phi}|_{r=r_s}. \quad (18)$$

We removed the mean-field contribution ( $m = 0$ ) and summed over all other  $m$ . Because of our wedge approach,  $l = 4$  is the lowest possible  $l$ . We refer to Viviani et al. (2018) and Käpylä et al. (2019) for details of computing spherical harmonic decompositions from simulations of the presented type.

For low  $l$ , the kinetic energy spectra (Fig. 8a) are similar for all runs – only the hydro runs have slightly higher energies. At the highest resolutions and  $l > 50$ , the velocity develops an inertial range, which can be best described by a power law of  $l^{-11/5}$ , as illustrated by the compensated spectrum in the inset. This power law was predicted by Bolgiano (1959) and Oboukhov (1959), and was also found in Käpylä (2021). However, as discussed in several studies (e.g., Brandenburg 1992; Rieutord & Rincon 2010; Xie & Huang 2022; Alam et al. 2023), this scaling was obtained for stably stratified media, but not for rotating convection. Moreover, the Bogliani-Obukhov scaling should only appear for those larger scales, which are influenced by the gravity-induced anisotropy, while being followed by a standard Kolmogorov scaling for smaller scales. Furthermore, we observe an extended inertial range only at the highest resolutions, as viscous diffusion affects all  $l$  otherwise.

For the magnetic spectra (Fig. 8b), the energies are very similar for all M runs at low  $l$ . 4M alone has a lower power at  $l < 10$ , which might be caused by some data loss<sup>2</sup>. We do not observe an inertial range with a clear power law, as in the H runs. For the S runs, the energies are lower at all scales than for the corresponding M runs. However, Run 4S has a higher power than the other S runs, however, in particular at low  $l$ , but it appears to be indistinguishable from Run 4M for  $l > 100$ . That the field in the S runs is lower than in the M runs, in particular at low  $l$ , is consistent with nearly the entire field at  $l > 500$  being due to the SSD, whereas tangling is dominant at  $l < 500$  for the highest  $\text{Re}_M$ . Surprisingly, the shapes of the spectra of the M and S runs are similar in general, which implies that the spectral properties of LSD- and SSD-generated fields are very similar, at least for  $l \geq 4$ . We only observe that amplitude differences are more pronounced at  $l < 100$ .

To investigate whether the magnetic field reaches superequipartition at certain scales, we also examined the ratio of the magnetic and kinetic spectra near the surface, as shown in Fig. 8c. Superequipartition is achieved (around  $l \sim 1000$ ) only in Run 3S, whereas the corresponding M run has a maximum energy ratio of 0.6. The lowest diffusivity runs only achieve just equipartition for  $600 < l < 2000$ . We note that these spectra were taken close to the surface, where the horizontally averaged magnetic field is well below equipartition, as shown in Fig. 7. We would expect the spectral ratio at larger depths to be higher. The fanning of the spectra, particularly at high  $l$  in the kinetic ones, is

<sup>2</sup> Unfortunately, we lost the data slices of Run 4M, so we used some early slices from Run 4M2, where the mean field was removed, but not all large-scale fields had decayed yet.

related to inaccuracies resulting from employing spherical harmonic decomposition on a spherical grid with an incomplete  $\theta$  range.

To show the Re dependence of the spectral energy more clearly, we plot for  $l = 10$  and 100 the kinetic and magnetic energy as function of Re for all runs (see Fig. 8d). The kinetic energy for  $l = 10$  appears to decrease mildly with increasing Re. Interestingly, this is not only the case for the M or S runs, but also for the H runs and hence cannot be due to a suppression by the magnetic field, as claimed in HK21. The magnetic energy at  $l = 10$  of the M runs seems to be independent of Re, except for a mild decrease for the highest Re. A strong increase is seen only for the S runs. The kinetic and magnetic energy at  $l = 100$  increase continuously. The kinetic energy alone seems to saturate for the highest Re. For this scale, the strong SSD in the highest Re runs has no marked influence on the kinetic energies.

When we compare our results with the spectra provided by HK21 and HKS22, we find two main differences: They observed superequipartition fields at small scales ( $l > 100$ ) even for their lowest resolution (similar to our Set 2). Additionally, the kinetic energy at large scales is suppressed in their results at high Re because of, as they interpreted it, their very strong SSD. We observe a small decrease in the large-scale energy, but this is also evident in the hydrodynamic runs. It is important to note that HK21 and HKS22 only studied one purely hydrodynamic run, and therefore, there is no Re dependence in their case. Furthermore, their simulations only developed an SSD but no LSD, which means that the influence of a large-scale field on the dynamics was not studied. The differences in the spectral properties might also be related to these two main distinctions in the setup, as discussed above.

### 3.5. Differential rotation and its generators

Next, we examined the profiles of differential rotation  $\Omega = \Omega_0 + \bar{u}_\phi/r \sin \theta$ , as shown in Figs. 9 and 10, and investigated the influence of the magnetic fields on their generation terms (see Figs. 11 and 12). As observed from the energy analysis, the differential rotation is most pronounced in the H runs and is suppressed in the M and S runs.

In the H runs, the contours of constant angular velocity tend to become more cylindrical toward the more turbulent regime, while the maximum  $\Omega$  values remain roughly constant across Runs 0H, 1H, and 2H. However, for the highest Re (Run 3H), the differential rotation is slightly weaker than in Run 1H. With increasing Re, more jets of opposite sign become visible. Surprisingly, the contours in Run 0H are far less cylindrical than in the H runs with higher Re. We attribute this to the absence of Busse columns (or banana cells) at the lowest Re, as illustrated in Fig. C.1.

As noted previously, the M runs consistently exhibit a weaker differential rotation with  $\Omega$  profiles strongly influenced by the magnetic field. We observe a tendency for the isorotation contours to become less cylindrical with higher Re. Except for some local minima and maxima near the poles, the differential rotation becomes much weaker in the highly turbulent regime than in the less turbulent regime. Additionally, the differential rotation profile in all cases with active SSD becomes increasingly hemispherically asymmetric with rising Re. This is attributable to the hemispherically asymmetric magnetic field. Notably, the minimum of  $\Omega$  at mid-latitudes nearly vanishes in the high-Re M runs. For the S runs, the profiles at weak SSD (Run 2S) resemble those of Run 2H. However, Run 3S with stronger SSD exhibits a weaker differential rotation, similar to Run 3M. The profiles of Runs 4S and 4M are almost the same. This might be related to the issues of these runs discussed in Sect. 3.2.

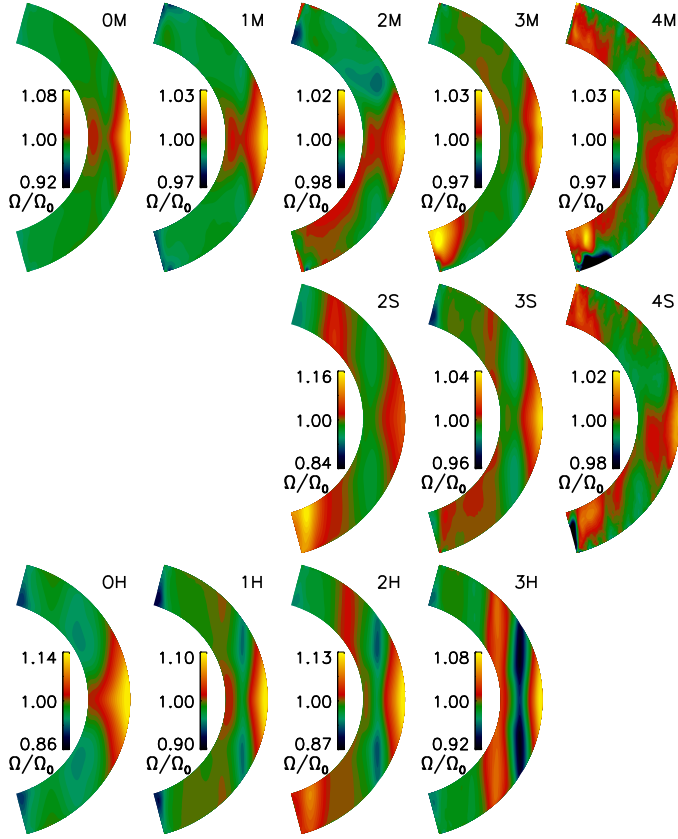


**Fig. 9.** Differential rotation  $\Omega/\Omega_0$ , with  $\Omega = \Omega_0 + \bar{u}_\phi/r \sin \theta$  for all runs.

The changes in the differential profile with  $Re$  and the presence of the two dynamos become clearer in the plots of the latitudinal distribution and  $Re$  dependence (Fig. 10) of  $\Omega$ . It is evident that it significantly decreases near the equator with increasing  $Re$  and in the presence of a magnetic field. Moreover, the jets present in the H runs at mid-latitudes are completely suppressed in the M runs. Interestingly, the differential rotation at the equator is already strongly suppressed in Run 2M, where the SSD is relatively weak, indicating that the suppression is due to the magnetic field generated by the LSD rather than the SSD. However, the SSD in Run 4S is capable of suppressing and shaping the differential rotation, similarly to its corresponding Run 4M.

The reduction of shear at high  $Re_M$  was also reported by Käpylä et al. (2017a). HK21 and HKS22 found that the differential rotation at high  $Re_M$  is also strongly influenced by the magnetic field, which is consistent with our work. However, in their cases, the magnetic field was solely due to an SSD, whereas in our case, the change in differential rotation is mainly due to the LSD.

Our modeling strategy prevented us from inspecting the actual generation process of the differential rotation profiles because we restarted from earlier models. We can therefore only address the relaxed states reliably.

The differential rotation follows the mean angular momentum balance (see, e.g. Rüdiger 1989),

$$\partial_t (s^2 \bar{\rho} \Omega) = -\nabla \cdot s \left[ s \bar{\rho} \bar{u} \Omega + (\bar{\rho} u)' u'_\phi - 2 \gamma \bar{\rho} \bar{\mathbf{S}} \cdot \hat{\mathbf{e}}_\phi - \mu_0^{-1} (\bar{\mathbf{B}} \bar{B}_\phi + \bar{\mathbf{B}}' \bar{B}'_\phi) \right], \quad (19)$$

where  $s = r \sin \theta$  is the lever arm. As usual, we neglected the compressible term related to  $\bar{\rho}' \bar{\mathbf{S}}$  in the equation above.

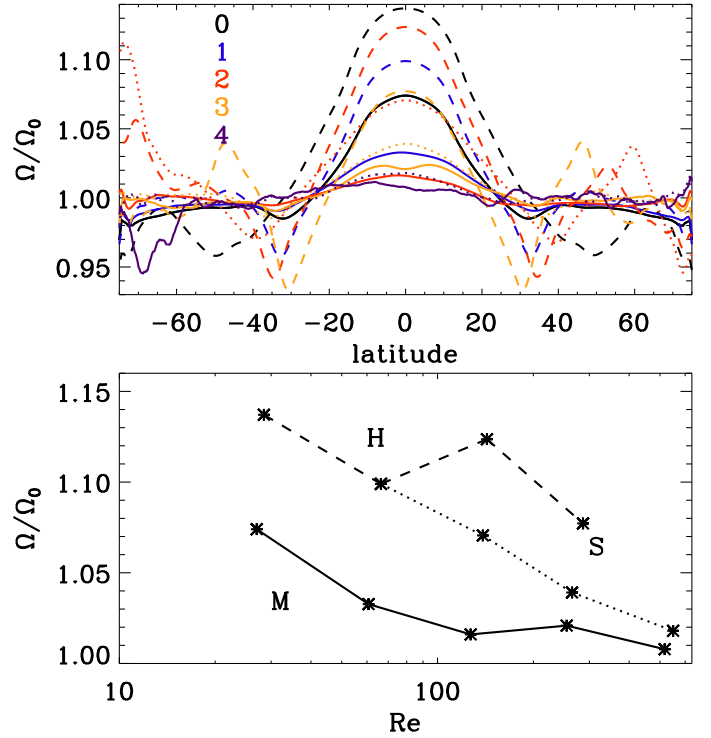


**Fig. 10.** Differential rotation of all runs near the surface ( $r = 0.98 R$ ). At the top we plot  $\Omega/\Omega_0$  as function of latitude. As before, the solid lines show M runs, dotted lines show S runs and the dashed lines show H runs, while the colors indicate the run sets with different  $Re$ . At the bottom, we plot  $\Omega/\Omega_0$  at the equator ( $\theta = \pi/2$ ) as a function of  $Re$ .

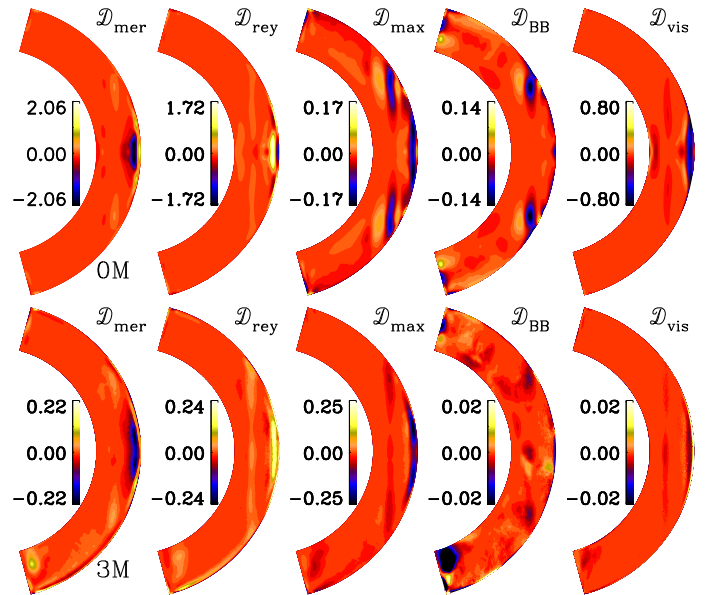


**Fig. 11.** Time-averaged contributions to the differential rotation energy evolution for Runs 0M and 3M, as given in Eqs. (21)–(25). The contributions are shown in units of  $J/m^3 s$ .

To determine which part of the angular momentum flux contributes significantly to the differential rotation, we calculated the contributions to the evolution of differential rotation energy density. This approach has the advantage that generating contributions are shown as positive values, and destructing ones as



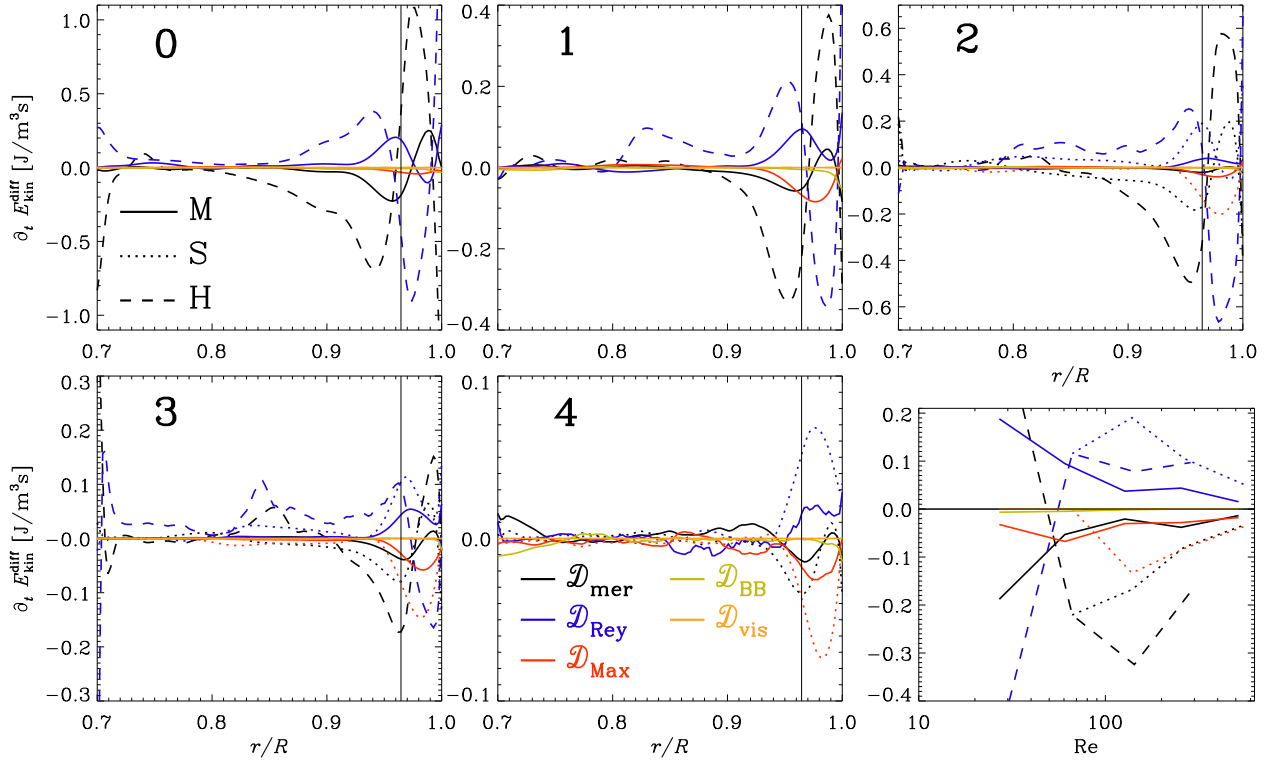


**Fig. 12.** Contributions to the differential rotation energy evolution averaged in time and latitude for all run sets (0 – 4) as functions of  $r/R$  (see Eqs. (21)–(25)). The bottom rightmost panel shows the contributions as functions of  $Re$  at  $r/R = 0.96$  (the vertical line in the other panels).

negative,

$$\partial_t E_{\text{kin}}^{\text{diff}} = (\bar{u}_\phi/s) \partial_t (s^2 \bar{\rho} \Omega) = \frac{1}{2} \partial_t (\bar{\rho} \bar{u}_\phi^2) = \mathcal{D}. \quad (20)$$

Using the right-hand side of Eq. (19) and also averaging over time, we can divide  $\mathcal{D}$  into five different contributions:

$$\mathcal{D}_{\text{Mer}} = -(\bar{u}_\phi/s) \nabla \cdot (s^2 \bar{\rho} \bar{u} \Omega) \quad \text{meridional circulation,} \quad (21)$$

$$\mathcal{D}_{\text{Rey}} = -(\bar{u}_\phi/s) \nabla \cdot (s(\bar{\rho} \bar{u})' \bar{u}_\phi') \quad \text{Reynolds stress,} \quad (22)$$

$$\mathcal{D}_{\text{Max}} = (\bar{u}_\phi/s) \nabla \cdot (s \mu_0^{-1} \bar{\mathbf{B}}' \bar{B}_\phi') \quad \text{SS Maxwell stress,} \quad (23)$$

$$\mathcal{D}_{\text{BB}} = (\bar{u}_\phi/s) \nabla \cdot (s \mu_0^{-1} \bar{\mathbf{B}} \bar{B}_\phi) \quad \text{LS Maxwell stress,} \quad (24)$$

$$\mathcal{D}_{\text{vis}} = (\bar{u}_\phi/s) \nabla \cdot (2s \nu \bar{\rho} \bar{\mathbf{S}} \cdot \hat{\mathbf{e}}_\phi) \quad \text{viscous stress.} \quad (25)$$

Due to our choice of azimuthal averages written out at run time, we calculated  $\mathcal{D}_{\text{Mer}}$  and  $\mathcal{D}_{\text{Rey}}$  slightly differently. However, their sum remains the same. For  $\mathcal{D}_{\text{Mer}}$ , we used

$$\nabla \cdot (s^2 \bar{\rho} \bar{u} \Omega) \approx \nabla \cdot (s^2 \bar{\rho} \bar{u} \Omega) + \nabla \cdot (s^2 \bar{\rho}' \bar{u}' \Omega_0), \quad (26)$$

where the second term was calculated by  $-s^2 \Omega_0 \nabla \cdot (\bar{\rho} \bar{u})$  using the conservation of mass flux,

$$\nabla \cdot (\bar{\rho} \bar{u}) = \nabla \cdot (\bar{\rho}' \bar{u}') + \nabla \cdot (\bar{\rho} \bar{u}) = 0. \quad (27)$$

For  $\mathcal{D}_{\text{Rey}}$  we used

$$\nabla \cdot (s(\bar{\rho} \bar{u})' \bar{u}_\phi') \approx \nabla \cdot (s \bar{\rho} \bar{u} \bar{u}_\phi') - \nabla \cdot (s \bar{\rho}' \bar{u}' \bar{u}_\phi). \quad (28)$$

Our choice at the end means that the term  $\nabla \cdot (s \bar{\rho}' \bar{u}' \bar{u}_\phi')$  is included in  $\mathcal{D}_{\text{Rey}}$  instead of in  $\mathcal{D}_{\text{Mer}}$ , and their sum is therefore the same as in the definitions Eqs. (21) and (22).

We show the time-averaged contributions exemplarily for Runs 0M and 3M as a meridional plot in Fig. 11 and for all runs as a line plot from additional averaging over latitude in Fig. 12. For all low  $Re$  runs, the main balance is between the contributions of meridional circulation  $\mathcal{D}_{\text{Mer}}$  and Reynolds stresses  $\mathcal{D}_{\text{Rey}}$ , with a small contribution of  $\mathcal{D}_{\text{vis}}$ . For most of the domain,  $\mathcal{D}_{\text{Rey}}$  is generative, whereas  $\mathcal{D}_{\text{Mer}}$  is destructive. At high  $Re$ , this balance still holds for the H runs, where  $\mathcal{D}_{\text{vis}}$  becomes increasingly smaller. For the M runs, we find two main channels through which the magnetic field influences the angular momentum. On one hand, the magnetic field suppresses  $\mathcal{D}_{\text{Mer}}$  and  $\mathcal{D}_{\text{Rey}}$  to much lower levels, accompanied by some changes in the spatial distribution. On the other hand, the contribution from small-scale Maxwell stresses  $\mathcal{D}_{\text{Max}}$  becomes comparable to  $\mathcal{D}_{\text{Rey}}$ , but has mostly negative values. It therefore compensates for  $\mathcal{D}_{\text{Rey}}$ . Surprisingly, this already occurs at  $Re \sim 60$ , where no SSD is present. The direct influence of the large-scale magnetic field ( $\mathcal{D}_{\text{BB}}$ ) appears to be significant only near the surface at high  $Re$ , where it has a destructive effect. For the S runs, the contribution of  $\mathcal{D}_{\text{Rey}}$  is not as effectively quenched as in the corresponding M runs. The magnetic influence primarily comes through the  $\mathcal{D}_{\text{Max}}$  contribution, which has a destructive effect throughout most of the convection zone. Together with the destructive contribution of  $\mathcal{D}_{\text{Mer}}$ , it balances  $\mathcal{D}_{\text{Rey}}$ .

From this differential rotation energy balance, we can deduce why the differential rotation is mostly quenched by the LSD and not the SSD alone. The quenching of  $\mathcal{D}_{\text{Rey}}$  appears to play an important role here. Only the large-scale field can effectively quench this contribution, thus preventing the development of strong differential rotation. Additionally, the small-scale magnetic field, whether generated by tangling or by an SSD, creates a destructive term,  $\mathcal{D}_{\text{Max}}$ , which further suppresses the generation of differential rotation.

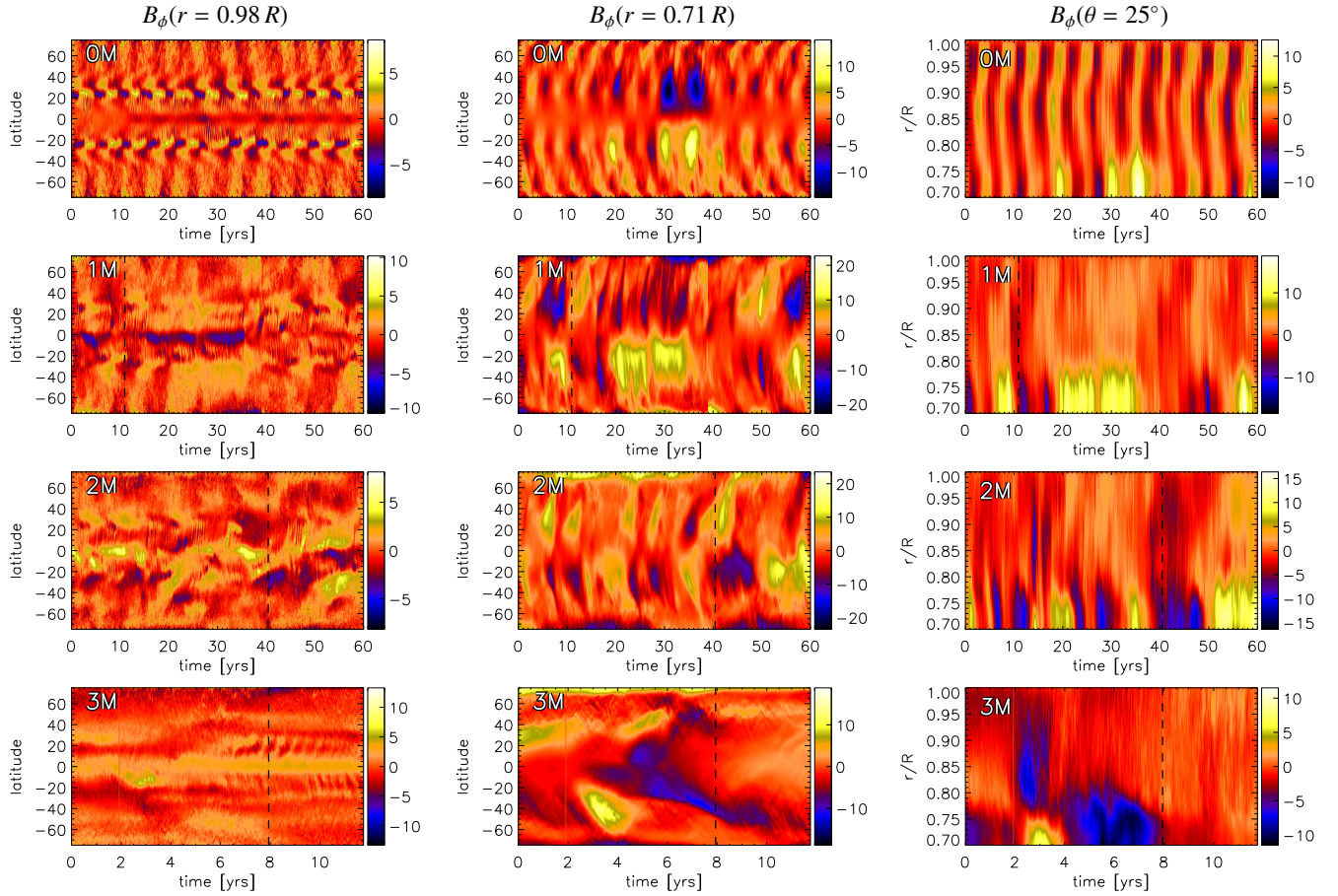


**Fig. 13.** Time evolution of the mean toroidal magnetic field  $\bar{B}_\phi$  for all M runs (except 4M and 4M2). We show time-latitude (butterfly) diagrams at  $r = 0.98 R$  (first column) and at  $r = 0.71 R$  (second column), and the time-radius diagram at  $25^\circ$  latitude (north). We note that the timescale for the first three rows is the same, but is different for the last one. The vertical dashed lines indicate the starting point from which we use a time interval to compute the time averages used in the analysis throughout this paper. The vertical stripes in Run 3M are due to data loss. The mean field is in units of kG.

In theory, Maxwell stresses could also act similarly to Reynolds stresses in generating differential rotation; we found that their contribution is always destructive, however. Previous studies by Käpylä et al. (2017a) showed that the contribution of the Reynolds stress is balanced by the contribution of meridional circulation, and that this balance shifts to a balance of Reynolds and Maxwell stress contributions. This finding was confirmed by HK21 and HKS22. However, the latter authors mostly attributed this change in balance to the presence of an SSD, whereas we find that this is already the case at moderate  $\text{Re}_M$ , where no SSD is present.

The finding that large-scale magnetic fields suppress differential rotation dates back to early magnetoconvection models (e.g. Gilman 1983), but also to many theoretical calculations. Quenching of the  $\Lambda$  effect by magnetism was intensively studied in mean-field models (e.g. Kitchatinov et al. 1994a; Kitchatinov 2016; Pipin 2017) and was also confirmed by numerical simulations (Käpylä et al. 2004; Käpylä 2019b). However, the magnetic field will also affect the turbulent viscosity in these mean-field models (e.g. Kitchatinov et al. 1994b), and therefore, differential rotation can also be enhanced (Kitchatinov 2016). Quenching of the  $\Lambda$  effect by SSD was found to be milder than by a corresponding large-scale magnetic field with the same strength in simplified numerical simulations (Käpylä 2019c).

The importance of Busse columns (or banana cells) for the generation of differential rotation was previously pointed out by

other authors (e.g. Hotta et al. 2015; Featherstone & Hindman 2016; Matilsky et al. 2020; Bekki et al. 2022; Käpylä 2023). One of their interpretations is that the prominent presence of these large-scale convective structures in simulations hinders the reproduction of the differential rotation of the Sun. Our results are in line with this interpretation because the banana cells seem to cause the differential rotation profile to become more cylindrical, whereas the contours of the Sun’s differential rotation are radial over a considerable range of mid-latitudes (e.g. Schou et al. 1998).

### 3.6. Magnetic field generation

Next, we studied the evolution of the mean toroidal magnetic field  $\bar{B}_\phi$ . We plot in Fig. 13 the butterfly diagrams of Runs 0M, 1M, 2M and 3M; for Run 4M, the time series is too short to form a meaningful diagram. Run 0M shows a very similar mean field evolution as the run of Käpylä et al. (2016): a regular cycle with equatorward migration throughout the convection zone, a fast cycle with poleward migration near the surface close to the equator, and a long cycle that is most pronounced at the bottom of the domain and capable of disturbing the other cycles. This is expected as 0M has the same parameters as the run of Käpylä et al. (2016), except for the use of a Kramers-based heat conduction instead of a prescribed conductivity profile. The dynamo mode with equatorward migration that was first reported



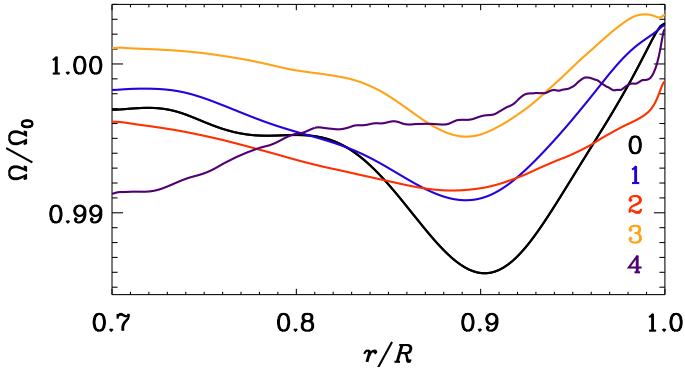


**Fig. 14.** Radial profile of the differential rotation  $\Omega/\Omega_0$  of all M runs. We show the radial profile at  $25^\circ$  latitude, which coincides with the local minimum of  $\Omega$ , causing the equatorward migrating magnetic field pattern in Run 0M.

in Käpylä et al. (2011b) and further discussed in Käpylä et al. (2013) can clearly be explained by an  $\alpha\Omega$  Parker dynamo wave (e.g. Warnecke et al. 2014, 2018). However, to obtain the exact period, many other turbulent transport coefficients have to be considered (Warnecke et al. 2021). The fast poleward dynamo mode could be identified as being of  $\alpha^2$  type (Käpylä et al. 2016; Warnecke et al. 2021), while the type of the long-period mode is currently unclear (Käpylä et al. 2016; Gent et al. 2017).

When  $Re$  and  $Re_M$  are increased, the dynamo solutions are affected: The clear equatorward migration vanishes for all runs starting from 1M. This is most likely due to changes in the differential rotation profile (see the discussion below). The two other modes still exist in the higher  $Re_M$  regime, however. For the highest values of  $Re_M$  (4M), the time series is unfortunately too short to identify the dynamo cycles safely. The fast dynamo mode is clearly visible in the 1M and 2M runs as well, and even in the 3M run. That this mode is still visible in Run 3M as well supports our interpretation that this is an  $\alpha^2$  type dynamo because, as discussed in Sect. 3.5, the differential rotation becomes very weak at these high  $Re_M$ . The long-cycle dynamo mode is rather irregular and mostly pronounced in field strength, but it also develops polarity reversals. Comparing the butterfly diagrams of 1M and 2M, we find that they look very similar, in particular near the bottom of the domain and at higher latitudes. In summary, an increase in the Reynolds numbers does not strongly affect the short and long cycles, which still generate significant mean magnetic fields, but it causes the equatorward migrating medium-length mode to vanish.

To investigate why this mode vanishes, we inspected the changes in the differential rotation profile in more detail roughly at the latitudinal and radial locations at which the previously found equatorward migrating dynamo mode is generated (see Fig. 14). The minimum of  $\Omega$  at  $r = 0.9$  and  $25^\circ$  latitude is very pronounced in the 0M run, it is already much weaker in 1M and 2M, but it has vanished completely in the run with the highest  $Re_M$  (3M). This fits our hypothesis well that the negative shear in this region generates the equatorward migrating dynamo mode seen in 0M (Warnecke et al. 2014, 2018); accordingly, when the shear is sufficiently weakened, this dynamo mode vanishes. To determine which dynamo is at work in these simulations, we need to measure the turbulent transport coefficients as in Warnecke et al. (2018) and analyze them via a mean-field model as in Warnecke et al. (2021). This analysis is currently under development and will be presented in a possible follow-up study.

To inspect at which locations the LSD and the SSD operate in our runs, we show in Fig. 15 meridional plots of the azimuthally averaged magnetic energy density of the mean and fluctuating fields separately. We recall that the magnetic fluctuations in Runs 0M and 1M are entirely generated by the tangling of the large-scale field, because no SSD operates in these runs. In Run 0M, the large-scale field is mostly generated at medium to high latitudes near the middle of the convection zone, which is consistent with earlier findings of runs with similar parameters (Warnecke et al. 2014, 2018; Käpylä et al. 2016). The weaker field near the bottom of the domain causes the long-term variation shown in Fig. 13. The corresponding small-scale field is also located at medium to high latitudes, as to be expected from the large-scale field. However, near the bottom of the domain, no small-scale field is generated because the convective motions in this area are weak (see Sect. 3.3). For the M runs with higher  $Re_M$ , the mean field at medium latitudes gradually vanishes and instead becomes dominant near the bottom of the domain. The small-scale field for small  $Re_M$  is mostly located at high latitudes, but it gradually becomes stronger near the equator. This increase is partly due to tangling as in 1M, but in particular for higher  $Re_M$  because the SSD operates in this area, as seen in Runs 2S and 3S. At the locations where the small-scale field is strong, the enthalpy flux and the kinetic energy also reach a maximum, as shown in Fig. 16 for the enthalpy flux  $\bar{F}_{\text{enth}}$ . Such a concentration of  $\bar{F}_{\text{enth}}$  near the equator was also observed in Käpylä et al. (2019) and Viviani & Käpylä (2021). The maximum of the small-scale field in these areas is therefore probably due to the enhanced convective motions. However, this is only true for the S runs. In the M runs, the situation is slightly different. In Run 2M, where an SSD is already present, we indeed see a concentration of small-scale field near the equator, similar to 2S, but also at higher latitudes, where the large-scale field is strong. The small-scale field still seems to be connected with the entropy flux, as the distribution of  $\bar{\mathbf{B}}'^2$  resembles the distribution of  $\bar{F}_{\text{enth}}$ .

For the high- $Re_M$  runs (3M and 4M), the small-scale field is not concentrated near the equator, as might be expected from their corresponding S runs. However, the distribution of  $\bar{\mathbf{B}}'^2$  here also somewhat resembles the distribution of  $\bar{F}_{\text{enth}}$ , at least in terms of a minimum near the equator.

Furthermore, even though the mean field is very strong near the bottom of the domain, the small-scale field is nearly zero. This is most likely due to the lack of strong convective motions there. We can explain the strong mean field at the bottom with the possibility that the field is generated above and then transported down by turbulent pumping or diffusion, and it finally slowly diffuses into this nearly turbulence-free zone, where it can survive for a long time because of the lack of strong turbulent diffusion. As another possibility, the field can be generated locally by the very strong shear flow, which only needs a weak  $\alpha$  counterpart to form a dynamo loop.

In Runs 4M, 4M2, and 4S, both the mean field and the small-scale field are mostly concentrated in the northern hemisphere. This is probably due to the short integration time. However, even in these runs, a band of weak small-scale magnetic field appears near the bottom of the domain. Compared to Runs 2S and 3S, the SSD in 4S has a larger volume-filling factor in the northern hemisphere that spreads to higher latitudes and outside the tangent cylinder. To summarize, the SSD is mostly active near the equator in the S runs and 2M, but not in 3M and 4M. The  $\bar{F}_{\text{enth}}$

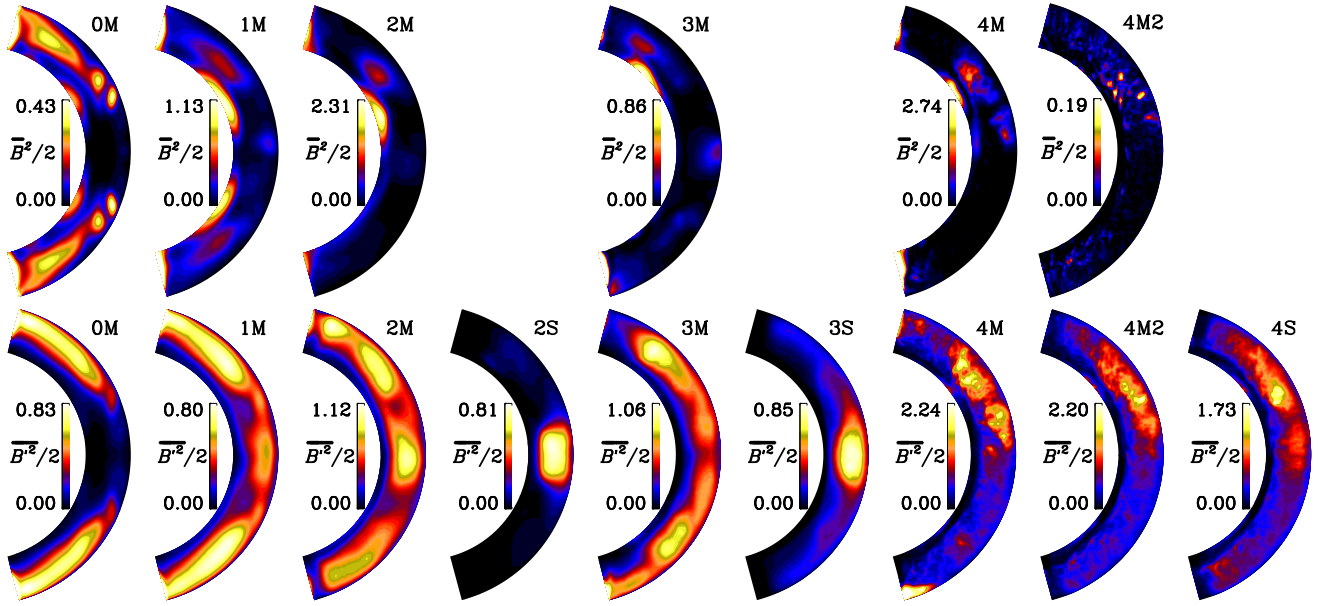


**Fig. 15.** Time-averaged mean magnetic energy of the mean fields  $\overline{B^2}/2$  (top row) and fluctuating fields  $\overline{B'^2}$  (bottom) for all M and S runs in units of  $10^5 \text{ J/m}^3$  for all magnetic runs (M+S). We disregard  $7^\circ$  near the latitudinal boundaries for determining the minimum and maximum values of the color range.

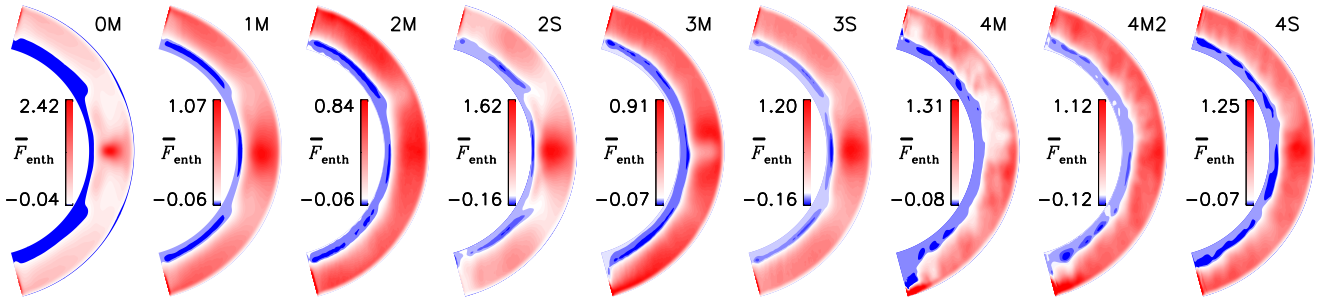


**Fig. 16.** Time-averaged radial enthalpy flux  $\overline{F}_{\text{enth}}$  normalized by the input flux  $\overline{F}_{\text{tot}}$  for all magnetic runs (M+S). For the color range see remark at Fig. 15.

and  $\overline{B'^2}$  distributions are similar, which indicates that SSD and tangling are both strong where the convection is strong.

### 3.7. Kinetic and current helicities

One of the most important turbulent dynamo processes is the  $\alpha$  effect (Steenbeck et al. 1966). Its strength can be estimated by the kinetic helicity density  $H_{\text{kin}} = \overline{\omega' \cdot \mathbf{u}'}$ ,  $\omega' = \text{curl } \mathbf{u}'$ , and the magnetic influence on it by the current helicity density  $H_{\text{curr}} = \overline{\mathbf{J}' \cdot \mathbf{B}'}/\mu_0 \bar{\rho}$  (e.g. Pouquet et al. 1976), here defined with a  $1/\bar{\rho}$  factor,

$$\alpha \approx -H_{\text{kin}}/3\tau_c + H_{\text{curr}}/3\tau_c, \quad (29)$$

where  $\tau_c$  is the turbulent correlation time, which in general does not need to be the same for the first and second term. In this work, we only studied these proxies (Figs. 17 and 18) and left the detailed analysis of the  $\alpha$  tensor and other turbulent transport coefficients to a future study.

As usual in rotating convection simulations,  $H_{\text{kin}}$  is predominantly negative in the upper half of the convection zone and positive below in the northern hemisphere while having the same pattern but opposite sign in the southern hemisphere (see Fig. 17). We find that the profile of  $H_{\text{kin}}$  is not much influenced by the increase in Re, nor does it show a large difference between

the S and M runs. Only the peak values of  $H_{\text{kin}}$  show a tendency to increase with increasing Re, and in Run 0M, the maxima near the equator extend farther into the convection zone.

The current helicity  $H_{\text{curr}}$  exhibits a different behavior. Similar to earlier results (e.g., Warnecke & Käpylä 2020), it is positive near the surface in the northern hemisphere, negative in the bulk, and again positive near the bottom of the domain for most of the M runs while having an analogous profile but with the opposite sign in the southern hemisphere. When Re is increased, it leaves the profile mostly unchanged, but leads to an increase in the peak values, at least when we compare 0M and 1M with 2M and 3M.

Interestingly, the current helicity  $H_{\text{curr}}$  (see Fig. 18) from the pure SSD runs follows the pattern of  $H_{\text{kin}}$  rather than that of  $H_{\text{curr}}$  of the corresponding M runs. The fact that the sign of  $H_{\text{curr}}$  is opposite in the cases with and without LSD is in line with the results of Warnecke et al. (2012), who explained this sign change from simulations (Warnecke et al. 2011) and observations (Brandenburg et al. 2011) by a simple model. This suggests that a sign change in  $H_{\text{curr}}$  is to be expected when an LSD is absent compared to when it is present.

$H_{\text{curr}}$  generated by the SSD is clearly lower than the one generated by an LSD. Furthermore,  $|H_{\text{curr}}|$  is always (except for 4M) lower than  $|H_{\text{kin}}|$ , and it is therefore not expected to influence the

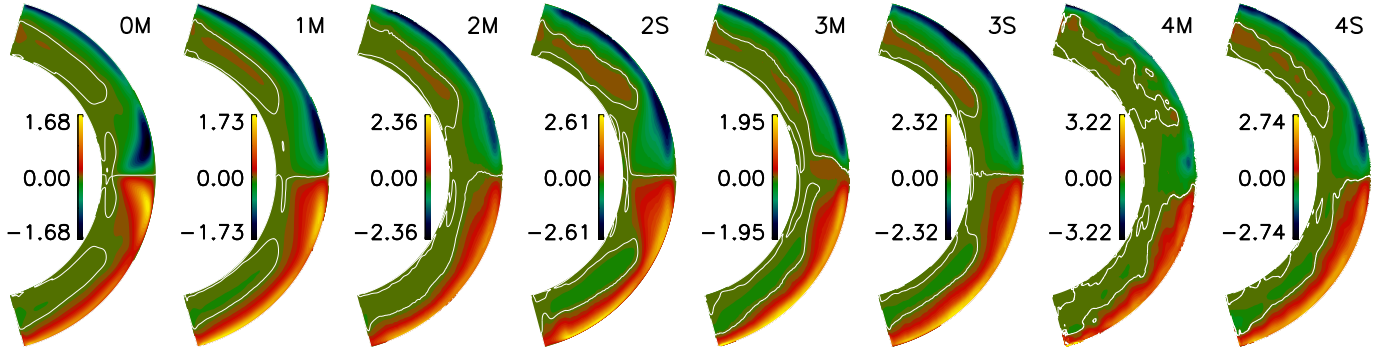


**Fig. 17.** Time-averaged kinetic helicity  $H_{\text{kin}} = \overline{\omega' \cdot \mathbf{u}'}$  in units of  $10^{-3} \text{ m/s}^2$  for the M and S runs. The white contours indicate zero values. We smoothed the data over 100 neighboring points for runs A4M and A4S for noise reduction.

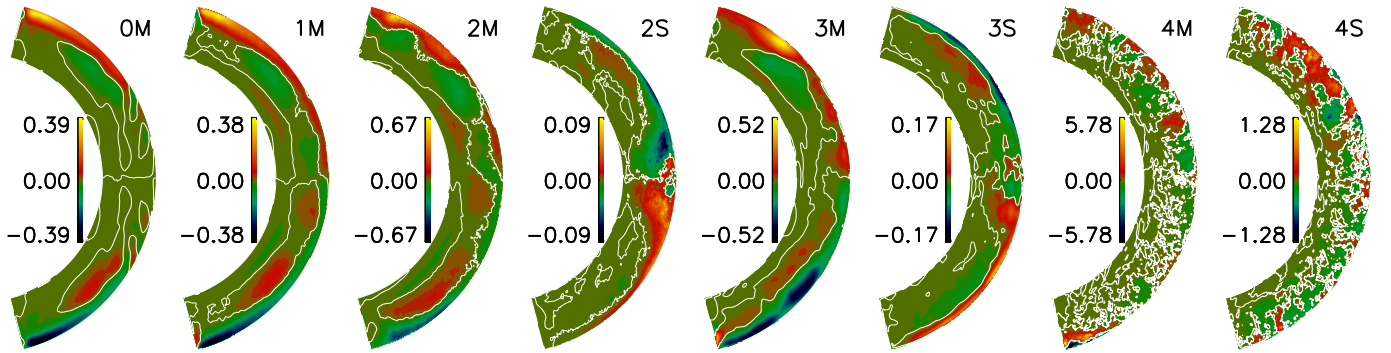


**Fig. 18.** Time-averaged current helicity  $H_{\text{curr}} = \overline{\mathbf{J}' \cdot \mathbf{B}'} / \mu_0 \bar{\rho}$  in units of  $10^{-3} \text{ m/s}^2$  for the M and S runs. The white contours indicate zero values. For data smoothing, see remark at Fig. 17.

$\alpha$  effect much, following Eq. (29). However, Warnecke & Käpylä (2020) showed that this approximation does not hold when comparing with  $\alpha$  determined by the test-field method when the magnitudes of  $H_{\text{curr}}$  and  $H_{\text{kin}}$  become comparable.

#### 4. Conclusions

We have conducted global convective dynamo simulations of solar-like stars, wherein we varied the viscosity, magnetic diffusivity, and SGS heat diffusivity to examine how the solutions depend on the fluid and magnetic Reynolds numbers. This enabled us to investigate the interaction between SSD and LSD and their effects on the overall dynamics. As a novel approach, we additionally investigated SSD in LSD-capable systems in isolation by suppressing the large-scale magnetic field.

As an outcome of these simulations, we identified the following results: Magnetic runs with  $\text{Re}_M \geq 140$  can excite an SSD, and its magnetic energy becomes comparable to that of the LSD at  $\text{Re}_M \approx 550$ . The total magnetic field energy appears to reach a maximum at  $\text{Re}_M = 120$  and decreases for runs with higher  $\text{Re}_M$ . Although the SSD becomes stronger at higher  $\text{Re}_M$ , the energy in the fluctuating field decreases mildly. As the mean field decreases by more than half compared to Runs 2M and 3M, the total magnetic energy is significantly weaker.

The scale of large-scale convective cells, also known as banana cells, does not depend on  $\text{Re}$  or on the presence of LSD or SSD. The depth of the subadiabatic layers is mostly independent of  $\text{Re}$ , except at mid-latitudes. However, the Deardorff zone becomes thinner, allowing for a thicker overshoot and radiative zone for higher  $\text{Re}$ . The turbulent velocity  $u'_{\text{rms}}$  increases with  $\text{Re}$  until  $\text{Re} = 120$ , after which it slightly decreases, even in the

H runs. This indicates that the decrease at high  $\text{Re}$  is not due to SSD or LSD, as found by HK21 and HKS22. The magnetic field in our simulations does not reach strong superequipartition with respect to turbulent kinetic energy. Additionally, at small scales, the magnetic field is mostly at subequipartition. Furthermore, the energy in the large convective scales mildly decreases with  $\text{Re}$ , but this occurs in the H runs as well, suggesting that it cannot be attributed to the effects of SSD or LSD.

Differential rotation is strongly quenched in M runs with high  $\text{Re}$ , primarily due to the magnetic field of LSD rather than of SSD. This agrees with many earlier analytical and numerical results (e.g. Gilman 1983; Kitchatinov et al. 1994a; Käpylä et al. 2004; Kitchatinov 2016; Pipin 2017; Käpylä 2019b). The magnetic field affects the angular momentum distribution via the suppression of the Reynolds stresses and the emergence of strong Maxwell stresses. The effects of the Maxwell stresses are dominated by the contributions of the small-scale fields, which are mostly due to tangling of the large-scale field and not the SSD, however. This contradicts the recent findings of (Hotta & Kusano 2021; Hotta et al. 2022), who argued that SSD is the most important driver of fluctuations and that through them, it affects the angular momentum balance.

The evolution of large-scale fields only shows a weak dependence on  $\text{Re}_M$ , with the equatorward migrating field mode disappearing for  $\text{Re}_M \geq 60$  due to the weaker shear at mid-latitudes. The irregular low-frequency mode at the bottom of the domain persists, and even the high-frequency mode near the surface is present in all relevant M runs. SSD is strongest in areas where the enthalpy flux is maximum, typically near the equator, where the turbulent energy reaches its peak. The profiles of kinetic and current helicity do not vary much with  $\text{Re}_M$ , but there is a tendency for a mild increase in their peak values with  $\text{Re}_M$ . Interestingly,



the current helicity generated by pure SSD has the opposite sign to that of LSD. Our work showed that it is important to study the SSD-LSD interaction to fully understand the dynamics in the Sun and other stars.

**Acknowledgements.** We thank the anonymous referee for their very useful comments and suggestions. The simulations have been carried out on SuperMUC-NG using the PRACE project Access Call 20 INTERDYNs project, on the Max Planck supercomputer at RZG in Garching and in the facilities hosted by the CSC-IT Center for Science in Espoo, Finland, which are financed by the Finnish ministry of education. This project has received funding from the European Research Council (ERC) under the European Union's Horizon 2020 research and innovation programme (grant agreement n:os 818665 "UniSDyn" and 101101005 "SYCOS"), and has been supported from the Academy of Finland Centre of Excellence ReSoLVE (project number 307411). This work was done in collaboration with the COFFIES DRIVE Science Center.

## References

- Alam, S., Verma, M. K., & Joshi, P. 2023, *Phys. Rev. E*, **107**, 055106
- Baliunas, S. L., Donahue, R. A., Soon, W. H., et al. 1995, *ApJ*, **438**, 269
- Barekat, A., & Brandenburg, A. 2014, *A&A*, **571**, A68
- Barik, A., Triana, S. A., Calkins, M., Stanley, S., & Aurnou, J. 2023, *Earth Space Sci.*, **10**, e2022EA002606
- Bekki, Y., Cameron, R. H., & Gizon, L. 2022, *A&A*, **666**, A135
- Bellot Rubio, L., & Orozco Suárez, D. 2019, *Liv. Rev. Sol. Phys.*, **16**, 1
- Bolignano, R., & J., 1959, *J. Geophys. Res.*, **64**, 2226
- Boro Saikia, S., Marvin, C. J., Jeffers, S. V., et al. 2018, *A&A*, **616**, A108
- Brandenburg, A. 1992, *Phys. Rev. Lett.*, **69**, 605
- Brandenburg, A. 2016, *ApJ*, **832**, 6
- Brandenburg, A., & Subramanian, K. 2005, *Phys. Rep.*, **417**, 1
- Brandenburg, A., Subramanian, K., Balogh, A., & Goldstein, M. L. 2011, *ApJ*, **734**, 9
- Brun, A. S., Strugarek, A., Noraz, Q., et al. 2022, *ApJ*, **926**, 21
- Busse, F. H. 1970, *J. Fluid Mech.*, **44**, 441
- Busse, F. H. 1976, *Icarus*, **29**, 255
- Chandrasekhar, S. 1961, *Hydrodynamic and Hydromagnetic Stability* (Oxford: Clarendon)
- Charbonneau, P. 2014, *ARA&A*, **52**, 251
- Fan, Y., & Fang, F. 2014, *ApJ*, **789**, 35
- Featherstone, N. A., & Hindman, B. W. 2016, *ApJ*, **818**, 32
- Gent, F. A., Käpylä, M. J., & Warnecke, J. 2017, *Astron. Nachr.*, **338**, 885
- Gilman, P. A. 1983, *ApJS*, **53**, 243
- Hanasoge, S. M., Duvall, T. L., & Sreenivasan, K. R. 2012, *Proc. Natl. Acad. Sci.*, **109**, 11928
- Hotta, H. 2017, *ApJ*, **843**, 52
- Hotta, H., & Kusano, K. 2021, *Nat. Astron.*, **5**, 1100
- Hotta, H., Rempel, M., & Yokoyama, T. 2015, *ApJ*, **798**, 51
- Hotta, H., Rempel, M., & Yokoyama, T. 2016, *Science*, **351**, 1427
- Hotta, H., Kusano, K., & Shimada, R. 2022, *ApJ*, **933**, 199
- Käpylä, P. J. 2019a, *A&A*, **631**, A122
- Käpylä, P. J. 2019b, *A&A*, **622**, A195
- Käpylä, P. J. 2019c, *Astron. Nachr.*, **340**, 744
- Käpylä, P. J. 2021, *A&A*, **655**, A78
- Käpylä, P. J. 2023, *A&A*, **669**, A98
- Käpylä, P. J., Korpi, M. J., & Tuominen, I. 2004, *A&A*, **422**, 793
- Käpylä, P. J., Mantere, M. J., & Hackman, T. 2011a, *ApJ*, **742**, 34
- Käpylä, P. J., Mantere, M. J., & Brandenburg, A. 2011b, *Astron. Nachr.*, **332**, 883
- Käpylä, P. J., Mantere, M. J., Cole, E., Warnecke, J., & Brandenburg, A. 2013, *ApJ*, **778**, 41
- Käpylä, P. J., Käpylä, M. J., & Brandenburg, A. 2014, *A&A*, **570**, A43
- Käpylä, M. J., Käpylä, P. J., Olsper, N., et al. 2016, *A&A*, **589**, A56
- Käpylä, P. J., Käpylä, M. J., Olsper, N., Warnecke, J., & Brandenburg, A. 2017a, *A&A*, **599**, A4
- Käpylä, P. J., Rheinhardt, M., Brandenburg, A., et al. 2017b, *ApJ*, **845**, L23
- Käpylä, P. J., Viviani, M., Käpylä, M. J., Brandenburg, A., & Spada, F. 2019, *Geophys. Astrophys. Fluid Dyn.*, **113**, 149
- Käpylä, P. J., Browning, M. K., Brun, A. S., Guerrero, G., & Warnecke, J. 2023, *Space Sci. Rev.*, **219**, 58
- Karak, B. B., Käpylä, P. J., Käpylä, M. J., et al. 2015, *A&A*, **576**, A26
- Kitchatinov, L. L. 2016, *Astron. Lett.*, **42**, 339
- Kitchatinov, L. L., Ruediger, G., & Kueker, M. 1994a, *A&A*, **292**, 125
- Kitchatinov, L. L., Pipin, V. V., & Rüdiger, G. 1994b, *Astron. Nachr.*, **315**, 157
- Mantere, M. J., Käpylä, P. J., & Hackman, T. 2011, *Astron. Nachr.*, **332**, 876
- Matilsky, L. I., Hindman, B. W., & Toomre, J. 2020, *ApJ*, **898**, 111
- Nelson, N. J., Brown, B. P., Brun, A. S., Miesch, M. S., & Toomre, J. 2013, *ApJ*, **762**, 73
- Oboukhov, A. 1959, *Akademiia Nauk SSSR Doklady*, **128**, 1246
- Olsper, N., Lehtinen, J. J., Käpylä, M. J., Pelt, J., & Grigorievskiy, A. 2018, *A&A*, **619**, A6
- Pencil Code Collaboration (Brandenburg, A., et al.) 2021, *JOSS*, **6**, 2807
- Pipin, V. V. 2017, *MNRAS*, **466**, 3007
- Pouquet, A., Frisch, U., & Léorat, J. 1976, *J. Fluid Mech.*, **77**, 321
- Rempel, M. 2014, *ApJ*, **789**, 132
- Rempel, M., Schüssler, M., & Knölker, M. 2009, *ApJ*, **691**, 640
- Rempel, M., Bhatia, T., Bellot Rubio, L., & Korpi-Lagg, M. J. 2023, *Space Sci. Rev.*, **219**, 36
- Rieutord, M., & Rincon, F. 2010, *Liv. Rev. Sol. Phys.*, **7**, 2
- Roberts, P. H. 1968, *Phil. Trans. R. Soc. London Ser. A*, **263**, 93
- Rüdiger, G. 1989, *Differential Rotation and Stellar Convection. Sun and Solar-type Stars* (Berlin: Akademie Verlag)
- Schekochihin, A. A., Haugen, N. E. L., Brandenburg, A., et al. 2005, *ApJ*, **625**, L115
- Schou, J., Antia, H. M., Basu, S., et al. 1998, *ApJ*, **505**, 390
- Singh, N. K., Rogachevskii, I., & Brandenburg, A. 2017, *ApJ*, **850**, L8
- Squire, J., & Bhattacharjee, A. 2015, *Phys. Rev. Lett.*, **115**, 175003
- Steenbeck, M., Krause, F., & Rädler, K.-H. 1966, *Z. Naturforsch. Teil A*, **21**, 369
- Stix, M. 2002, *The Sun: An Introduction* (Berlin: Springer)
- Tobias, S. M., & Cattaneo, F. 2013, *Nature*, **497**, 463
- Vainshtein, S. I., & Cattaneo, F. 1992, *ApJ*, **393**, 165
- Väisälä, M. S., Pekkila, J., Käpylä, M. J., et al. 2021, *ApJ*, **907**, 83
- Viviani, M., & Käpylä, M. J. 2021, *A&A*, **645**, A141
- Viviani, M., Warnecke, J., Käpylä, M. J., et al. 2018, *A&A*, **616**, A160
- Warnecke, J., & Käpylä, M. J. 2020, *A&A*, **642**, A66
- Warnecke, J., Brandenburg, A., & Mitra, D. 2011, *A&A*, **534**, A11
- Warnecke, J., Brandenburg, A., & Mitra, D. 2012, *JSWSC*, **2**, A11
- Warnecke, J., Käpylä, P. J., Mantere, M. J., & Brandenburg, A. 2013, *ApJ*, **778**, 141
- Warnecke, J., Käpylä, P. J., Käpylä, M. J., & Brandenburg, A. 2014, *ApJ*, **796**, L12
- Warnecke, J., Käpylä, P. J., Käpylä, M. J., & Brandenburg, A. 2016, *A&A*, **596**, A115
- Warnecke, J., Rheinhardt, M., Tuomisto, S., et al. 2018, *A&A*, **609**, A51
- Warnecke, J., Rheinhardt, M., Viviani, M., et al. 2021, *ApJ*, **919**, L13
- Warnecke, J., Korpi-Lagg, M. J., Gent, F. A., & Rheinhardt, M. 2023, *Nat. Astron.*, **7**, 662
- Xie, J.-H., & Huang, S.-D. 2022, *J. Fluid Mech.*, **942**, A19
- Yan, M., & Calkins, M. A. 2022, *J. Fluid Mech.*, **951**, A24

## Appendix A: Diffusivity profiles

To avoid numerical artifacts near the latitudinal boundaries, we apply a profile for the diffusivities  $\nu$  and  $\eta$ , increasing towards these boundaries. The profiles' shape is shown in Fig. A.1, it is determined by its width  $\Delta\theta_\nu$  and  $\Delta\theta_\eta$ , respectively, and the ratio between the boundary value and the value at the equator,

$$\Delta_{\nu\eta} \equiv \frac{\nu(\theta = \Theta_0, \pi - \Theta_0)}{\nu(\theta = \pi/2)} = \frac{\eta(\theta = \Theta_0, \pi - \Theta_0)}{\eta(\theta = \pi/2)}. \quad (\text{A.1})$$

We choose the minimal possible values for  $\Delta\theta_\nu$ ,  $\Delta\theta_\eta$ , and  $\Delta_{\nu\eta}$ , which keep the runs stable. It turns out that these adjustments are needed for runs with  $\text{Re} \geq 61$ , see Table 1 for details.

Furthermore, for high resolution simulations ( $\text{Re} \geq 260$ ), the runs have a tendency to produce vortex-like structures at high latitudes. They are as such an interesting phenomenon (Käpylä et al. 2011a; Mantere et al. 2011), but they decrease the time step significantly. Hence, we decided to suppress them in this work by choosing  $\Delta\theta_\nu = 17^\circ$  and postpone their detailed study to the future.

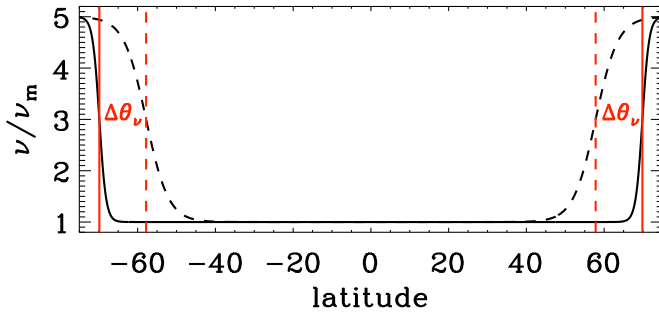


**Fig. A.1.** Latitudinal diffusivity profiles shown for viscosity  $\nu$  with width  $\Delta\theta_\nu = 5^\circ$  (solid line) and  $17^\circ$  (dashed), indicated by vertical red lines.  $\nu_m$  is the equatorial value of  $\nu$ .

## Appendix B: Slope-limited diffusion

Besides the constant diffusivity  $\nu$ , the H runs need additional explicit numerical diffusion to be stable. Our choice of using an enhanced luminosity at the bottom boundary, (see Käpylä et al. 2013, for details), causes the local Mach number  $\text{Ma} = |u|/c_s$  to increase near the surface to unusually high values. In the H runs, this can lead to numerical instabilities whereas the M and S runs are stable enough due to the presence of the magnetic field and hence do not need any additional diffusion. To let the numerical diffusion act only in regions, where it is needed, we employ slope-limited diffusion (SLD), newly implemented to the Pencil Code. It turns out that with our choice of parameters as specified below, we are able to stabilize the runs without influencing the overall dynamics much. In the following, we will briefly describe implementation and parameter choice. Thereby, we follow roughly Rempel et al. (2009) and Rempel (2014).

The main idea is to define the diffusive flux  $f$  of a velocity component  $u$  based on a slope limiter. At the cell interface  $k + 1/2$ , it is given by

$$f_{k+1/2} = -\frac{1}{2} c_{k+1/2}^{\text{sld}} Q_{k+1/2} (u_{k+1/2}^{\text{R}} - u_{k+1/2}^{\text{L}}), \quad (\text{B.1})$$

where the subscript  $k$  indicates the cell or grid-point in one particular coordinate direction,  $u_{k+1/2}^{\text{R}}$  and  $u_{k+1/2}^{\text{L}}$  are the right and left values at the cell interface of the velocity component and  $c^{\text{sld}}$

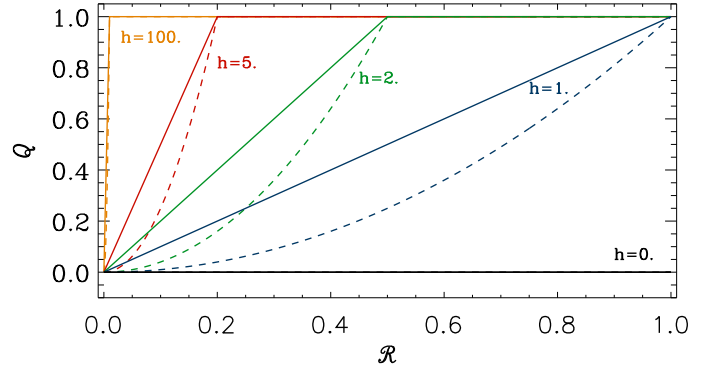


**Fig. B.1.** Visualization of Eq. (B.9):  $Q$  as function of the slope ratio  $\mathcal{R}$  for various  $h_{\text{sld}}$  (colored lines) with  $n_{\text{sld}}=1$  (solid) and  $n_{\text{sld}}=2$  (dashed).

is the characteristic speed, defined below.  $u^{\text{R}}$  and  $u^{\text{L}}$  are defined via

$$u_{k-1/2}^{\text{L}} = u_{k-1} + \Delta u_{k-1} \quad (\text{B.2})$$

$$u_{k-1/2}^{\text{R}} = u_k - \Delta u_k \quad (\text{B.3})$$

$$u_{k+1/2}^{\text{L}} = u_k + \Delta u_k \quad (\text{B.4})$$

$$u_{k+1/2}^{\text{R}} = u_{k+1} - \Delta u_{k+1} \quad (\text{B.5})$$

with the estimated slopes

$$\Delta u_k = \text{minmod}(u_k - u_{k-1}, u_{k+1} - u_k), \quad (\text{B.6})$$

where the minmod function is defined as

$$\text{minmod}(a, b) = \frac{1}{2} \text{sgn}(a) \max[0, \min(|a|, \text{sgn}(a)b)], \quad (\text{B.7})$$

meaning

$$\text{minmod}(a, b) = \begin{cases} +\frac{1}{2} \min(|a|, |b|) \\ 0 \\ 0 \\ -\frac{1}{2} \min(|a|, |b|) \end{cases} \quad \text{for} \quad \begin{cases} a > 0, b > 0 \\ a < 0, b > 0 \\ a > 0, b < 0 \\ a < 0, b < 0 \end{cases}. \quad (\text{B.8})$$

The diffusive flux is additionally adjusted by the factor

$$Q_{k+1/2}(\mathcal{R}_{k+1/2}) = [\min(1, h_{\text{sld}} \mathcal{R}_{k+1/2})]^{n_{\text{sld}}}, \quad (\text{B.9})$$

which controls its non-linearity by the power  $n_{\text{sld}}$  and has values between 0 and 1. The parameter  $h_{\text{sld}}$  sets the strength of the diffusion for a given slope. If  $h_{\text{sld}} = \infty$ , i.e.  $Q = 1$ , Eq. (B.1) represent a linear 2-order Lax-Friedrichs-scheme. The lower  $h_{\text{sld}}$ , the less diffusive is the scheme. The power  $n_{\text{sld}}$  can reduce the diffusion even further for small slopes. The slope ratio  $\mathcal{R}$  is defined as

$$\mathcal{R}_{k+1/2} = \frac{|u_{k+1/2}^{\text{R}} - u_{k+1/2}^{\text{L}}|}{|u_{k+1} - u_k|}. \quad (\text{B.10})$$

It relates the  $u$  difference at the cell interface to the difference between the cell centers, therefore indicating the relative slope strength. Equation B.9 implies that in regions where  $\mathcal{R}_{k+1/2} \geq 1/h_{\text{sld}}$ , the diffusive flux is maximal and for regions, where  $\mathcal{R}_{k+1/2} < 1/h_{\text{sld}}$  the diffusive flux is reduced, see Fig. B.1 for an illustration. In this work, we use  $h_{\text{sld}} = 2$  and  $n_{\text{sld}} = 1$  for the density and  $h_{\text{sld}} = 1$  and  $n_{\text{sld}} = 2$  for all velocity components. We note here that in Rempel et al. (2009) a similar scheme is used, which corresponds to  $h_{\text{sld}} = 1$  and  $n_{\text{sld}} = 2$ . In the work of Rempel (2014), a different expression for  $Q(\mathcal{R})$  is used – see

their Eq. (10), employing only one parameter instead of two. Detailed tests indicate no significant differences between his and our scheme.

The characteristic speed is derived from the signal (advection and wave) speeds in the system:

$$c^{\text{sld}} = w_{\text{hyd}}^{\text{sld}} |\mathbf{u}| + w_{\text{sound}}^{\text{sld}} c_s + w_{\text{mag}}^{\text{sld}} v_A, \quad (\text{B.11})$$

where  $v_A$  is the Alfvén speed, and the weights  $w_*^{\text{sld}}$  can be chosen depending on the nature of the problem. In this work, we set  $w_{\text{hyd}}^{\text{sld}} = 1$  and  $w_{\text{sound}}^{\text{sld}} = 0.001$ ; there is no magnetic contribution because we use SLD only for purely hydrodynamic runs. The intercell values of  $c^{\text{sld}}$  are calculated by linear interpolation:

$$c_{k+1/2}^{\text{sld}} = \frac{c_k^{\text{sld}} + c_{k+1}^{\text{sld}}}{2}. \quad (\text{B.12})$$

Connecting the strength of the SLD term to the signal speeds via  $c^{\text{sld}}$  makes an extra time step constraint unnecessary.

The calculation of the diffusive fluxes is now performed at each grid point for all three directions separately. With these three fluxes we can for a scalar quantity form a diffusive flux vector  $\mathbf{f}_{\text{sld}} = (f_q)$ , where  $q$  indicates the coordinate direction. If the diffusive fluxes are calculated for a vector quantity, then each vector component builds its own flux vector and these together form a diffusive flux tensor  $\mathcal{F}_{\text{sld}}$ .

Finally, the diffusive fluxes are added to the momentum and continuum equations via

$$\frac{D\mathbf{u}}{Dt} = \dots - \nabla^{\text{2nd}} \cdot \mathcal{F}_{\text{sld}}^{\mathbf{u}}, \quad \frac{D \ln \rho}{Dt} = \dots - \nabla^{\text{2nd}} \cdot \mathbf{f}_{\text{sld}}^{\rho}, \quad (\text{B.13})$$

where  $\mathcal{F}_{\text{sld}}^{\mathbf{u}}$  is the SLD tensor for the velocity and  $\mathbf{f}_{\text{sld}}^{\rho}$  is the SLD vector for the density. For simplicity, we use 2nd order finite differences for the divergence ( $\nabla^{\text{2nd}}$ ):

$$\nabla^{\text{2nd}} \cdot \mathbf{f}_{\text{sld}} = \sum_q \partial_q^{\text{2nd}} f_q = \sum_q \frac{f_q(q_{k+}) - f_q(q_{k-})}{q_{k+} - q_{k-}}, \quad (\text{B.14})$$

where  $\mathbf{f}_{\text{sld}}$  stands for  $\mathbf{f}_{\text{sld}}^{\rho}$  or for one of the column vectors of  $\mathcal{F}_{\text{sld}}^{\mathbf{u}}$  and  $q$  signifies the coordinate, i.e.  $x$ ,  $y$  or  $z$ .  $q_k$  denotes the grid point under consideration in the direction of the coordinate  $q$  and  $q_{k+}$  and  $q_{k-}$  are short for  $q_{k+1/2}$  and  $q_{k-1/2}$ , respectively. For brevity, we show only that argument of  $f_q$ , with respect to which the derivation is performed. For  $\mathcal{F}_{\text{sld}}^{\mathbf{u}}$ , we calculate the divergence analogously for each component.

For spherical coordinates, Eq. (B.14) is modified and reads for an SLD vector such as  $\mathbf{f}_{\text{sld}}^{\rho}$

$$\begin{aligned} \nabla^{\text{2nd}} \cdot \mathbf{f}_{\text{sld}} &= \frac{r_{k+}^2 f_r(r_{k+}) - r_{k-}^2 f_r(r_{k-})}{r_k^2 (r_{k+} - r_{k-})} + \frac{\sin(\theta_{k+}) f_\theta(\theta_{k+}) - \sin(\theta_{k-}) f_\theta(\theta_{k-})}{r_k \sin(\theta_k) (\theta_{k+} - \theta_{k-})} \\ &+ \frac{f_\phi(\phi_{k+}) - f_\phi(\phi_{k-})}{r_k \sin(\theta_k) (\phi_{k+} - \phi_{k-})} \end{aligned} \quad (\text{B.15})$$

for an SLD tensor such as  $\mathcal{F}_{\text{sld}}^{\mathbf{u}}$

$$\begin{aligned} [\nabla^{\text{2nd}} \cdot \mathcal{F}_{\text{sld}}]_r &= \frac{r_{k+}^2 f_r^r(r_{k+}) - r_{k-}^2 f_r^r(r_{k-})}{r_k^2 (r_{k+} - r_{k-})} \\ &+ \frac{\sin(\theta_{k+}) f_\theta^r(\theta_{k+}) - \sin(\theta_{k-}) f_\theta^r(\theta_{k-})}{r_k \sin(\theta_k) (\theta_{k+} - \theta_{k-})} \end{aligned} \quad (\text{B.16})$$

$$\begin{aligned} &+ \frac{f_\phi^r(\phi_{k+}) - f_\phi^r(\phi_{k-})}{r_k \sin(\theta_k) (\phi_{k+} - \phi_{k-})} \\ &- \frac{f_\theta^\phi(\theta_{k+}) + f_\theta^\phi(\theta_{k-})}{2r_k} - \frac{f_\phi^\phi(\phi_{k+}) + f_\phi^\phi(\phi_{k-})}{2r_k}, \end{aligned} \quad (\text{B.17})$$

$$\begin{aligned} [\nabla^{\text{2nd}} \cdot \mathcal{F}_{\text{sld}}]_\theta &= \frac{r_{k+}^2 f_r^\theta(r_{k+}) - r_{k-}^2 f_r^\theta(r_{k-})}{r_k^2 (r_{k+} - r_{k-})} \\ &+ \frac{\sin(\theta_{k+}) f_\theta^\theta(\theta_{k+}) - \sin(\theta_{k-}) f_\theta^\theta(\theta_{k-})}{r_k \sin(\theta_k) (\theta_{k+} - \theta_{k-})} \\ &+ \frac{f_\phi^\theta(\phi_{k+}) - f_\phi^\theta(\phi_{k-})}{r_k \sin(\theta_k) (\phi_{k+} - \phi_{k-})} - \frac{f_r^\phi(\theta_{k+}) + f_r^\phi(\theta_{k-})}{2r_k} \\ &- \frac{\cot(\theta_k) (f_\phi^\phi(\phi_{k+}) + f_\phi^\phi(\phi_{k-}))}{2r_k}, \end{aligned} \quad (\text{B.18})$$

$$\begin{aligned} [\nabla^{\text{2nd}} \cdot \mathcal{F}_{\text{sld}}]_\phi &= \frac{r_{k+}^2 f_r^\phi(r_{k+}) - r_{k-}^2 f_r^\phi(r_{k-})}{r_k^2 (r_{k+} - r_{k-})} \\ &+ \frac{\sin(\theta_{k+}) f_\theta^\phi(\theta_{k+}) - \sin(\theta_{k-}) f_\theta^\phi(\theta_{k-})}{r_k \sin(\theta_k) (\theta_{k+} - \theta_{k-})} \\ &+ \frac{f_\phi^\phi(\phi_{k+}) - f_\phi^\phi(\phi_{k-})}{r_k \sin(\theta_k) (\phi_{k+} - \phi_{k-})} - \frac{f_r^\phi(\theta_{k+}) + f_r^\phi(\theta_{k-})}{2r_k} \\ &- \frac{\cot(\theta_k) (f_\theta^\phi(\theta_{k+}) + f_\theta^\phi(\theta_{k-}))}{2r_k}, \end{aligned} \quad (\text{B.19})$$

where the superscripts of  $f$  indicate the quantity the diffusive flux is calculated for, e.g.  $r$  for  $u_r$ .

The viscous heat due to SLD,  $\mathcal{H}^{\text{sld}}$ , is defined at grid point  $k$  as

$$\begin{aligned} \mathcal{H}^{\text{sld}} &= \frac{1}{2} \sum_{p,q} \left\{ f_q^p(q_{k-}) \frac{\rho(q_k) u_p(q_k) - \rho(q_{k-1}) u_p(q_{k-1})}{q_k - q_{k-1}} \right. \\ &\quad \left. + f_q^p(q_{k+}) \frac{\rho(q_{k+1}) u_p(q_{k+1}) - \rho(q_k) u_p(q_k)}{q_{k+1} - q_k} \right\}. \end{aligned} \quad (\text{B.20})$$

where  $p, q$  denote the Cartesian coordinates. In spherical coordinates, this expression will be modified taking into account the appropriate derivatives. We note here that the viscous heating implementation in MURAM (Rempel et al. 2009; Rempel 2014) only takes into account the derivative of the velocity and not the momentum, i.e. it neglects the changes in the density.

Using a mass diffusion introduces an additional mass flux, for which we compensated in the momentum and energy equations.

## Appendix C: Spectra of banana cells

To investigate how the scales of the banana cells depend on the Reynolds numbers, we calculate the power spectra of the kinetic energy density of the radial flow,  $E_{\text{kin}}^r$ , near the surface ( $r = r_s \equiv 0.98 R$ ). For this, we cut out a thin latitudinal band around the equator ( $\pm 7.5^\circ$ ) and calculate the power spectrum of  $E_{\text{kin}}^r$ , averaged over latitude and time, as a function of the angular order  $m$  for each run. We rely on the definition

$$\begin{aligned} \sum_m \tilde{E}_{\text{kin}}^r(m) &= \frac{1}{2} \sum_m \left\langle \left| \text{FFT}[(u_r \sqrt{\rho})(r_s)](m) \right|^2 \right\rangle_{\theta t} \\ &= \frac{r_s}{2} \left\langle (u_r^2 \rho)(r_s) \right\rangle_{\theta \phi t}, \end{aligned} \quad (\text{C.1})$$



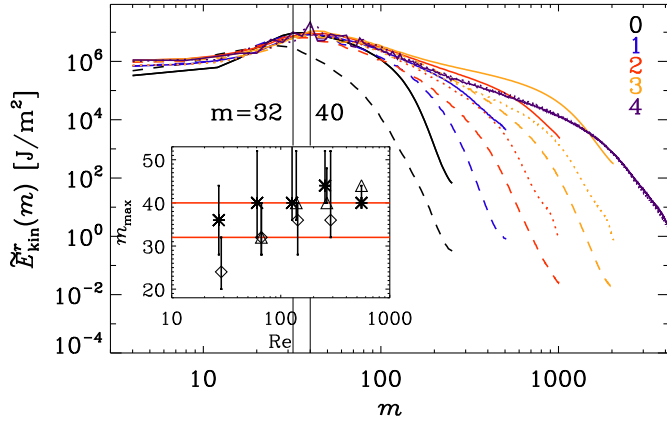


**Fig. C.1.** Longitudinal power spectra of the radial kinetic energy density,  $\tilde{E}_{\text{kin}}^r$ , near the surface  $r=0.98 R$  for a narrow latitudinal band around the equator ( $\pm 7.5^\circ$ ). The colors indicate the run sets and the line styles/symbols the run type: solid/asterisk (M), dashed/diamonds (H) and dotted/triangles (S). The spectra are averaged over the  $\theta$  bands and time. The inlay shows the  $m$  value of the maxima as a function of  $\text{Re}$  for all runs. The errors are calculated using an 80% range around the peak. The values  $m = 32$  and  $m = 40$  are indicated by black vertical and (in inlay) red horizontal lines, respectively.

where the tilde and the operator FFT indicate the Fourier transform. The spectra are shown in Fig. C.1 for all runs, including the  $\text{Re}$  dependence of the  $m$  of their maxima. Only a weak  $\text{Re}$  dependence is visible. The spectra of the M runs, except M0, peak around  $m = 40$ , whereas those of the H runs peak at slightly lower  $m \approx 32$ . The S run spectra peak at  $m = 32$  for moderate  $\text{Re}_M$  and at  $m = 40$  for high  $\text{Re}_M$ .